PHYSICAL REVIEW E **89**, 053320 (2014)

Phase-field-based multiple-relaxation-time lattice Boltzmann model for incompressible multiphase flows

H. Liang,[1] B. C. Shi,[2,*] Z. L. Guo,[1] and Z. H. Chai[2]
[1]*State Key Laboratory of Coal Combustion, Huazhong University of Science and Technology, Wuhan 430074, China*
[2]*School of Mathematics and Statistics, Huazhong University of Science and Technology, Wuhan 430074, China*
(Received 22 January 2014; published 30 May 2014)

In this paper, a phase-field-based multiple-relaxation-time lattice Boltzmann (LB) model is proposed for incompressible multiphase flow systems. In this model, one distribution function is used to solve the Chan-Hilliard equation and the other is adopted to solve the Navier-Stokes equations. Unlike previous phase-field-based LB models, a proper source term is incorporated in the interfacial evolution equation such that the Chan-Hilliard equation can be derived exactly and also a pressure distribution is designed to recover the correct hydrodynamic equations. Furthermore, the pressure and velocity fields can be calculated explicitly. A series of numerical tests, including Zalesak's disk rotation, a single vortex, a deformation field, and a static droplet, have been performed to test the accuracy and stability of the present model. The results show that, compared with the previous models, the present model is more stable and achieves an overall improvement in the accuracy of the capturing interface. In addition, compared to the single-relaxation-time LB model, the present model can effectively reduce the spurious velocity and fluctuation of the kinetic energy. Finally, as an application, the Rayleigh-Taylor instability at high Reynolds numbers is investigated.

DOI: 10.1103/PhysRevE.89.053320 PACS number(s): 47.11.−j, 47.55.−t, 68.03.−g

I. INTRODUCTION

Multiphase flows frequently occur in many important engineering and scientific applications, but modeling of such flows is a rather challenging task due to complex interfacial dynamics between different phases. Interface tracking is a widely used technique in multiphase flow models, which can be commonly classified into two categories: sharp interface methods [1,2] and diffuse interface methods [3,4]. In the sharp interface methods, different fluids are separated by the sharp interface and fluid properties such as density and viscosity at the interface are discontinuous. On the contrary, in the diffuse interface methods, the interface has a nonzero width and fluid properties vary smoothly across the interface. These features make the diffuse interface methods have some advantages over the sharp interface methods in the study of multiphase flows in which the interface undergoes a high deformation and even breaks up. Among the diffuse interface approaches, the lattice Boltzmann (LB) method [5–8] has received particular attention in that it can simulate multiphase flows effectively by incorporating the intermolecular interactions in a straightforward way.

Over the decades, several types of LB models for multiphase flows have been developed under different physical pictures. The first multiphase LB model is the color-gradient model proposed by Gunstensen *et al.* [9] based on a lattice gas method [10]. In this model, two colored particles are introduced to describe different fluids and the interparticle interactions are expressed by a local color gradient associated with the density difference. Subsequently, Shan and Chen [11,12] proposed another type of multiphase LB model, known as the pseudopotential model, by introducing an artificial interparticle potential to describe fluid interactions. This model gives a nonideal equation of state and has a capacity to simulate miscible or immiscible flows via controlling the interaction strength in a multiphase system [13]. With the idea of free energy, Swift *et al.* [14] constructed a third type of multiphase LB model in which a nonideal pressure tensor related to the free-energy functional was introduced. A limitation of the original model is the lack of Galilean invariance that was restored in the later developed free-energy models [15–17]. More recently, Inamuro *et al.* [18] proposed a free-energy-based model that can simulate multiphase flow with a large density ratio. Different from the above three types of models, some kinetic-based multiphase LB models were proposed based on the Enskog equation [19,20] and the modified Boltzmann equation [21]. These models usually have strong physical foundations owing to the underlying physics of the kinetic theory, but up to now, the practical applications of these models are still limited. He *et al.* [22] developed a more popular incompressible multiphase model, which is an extension of their former kinetic-theory-based model [21]. Different from the former model, a pressure distribution function was introduced in this model such that the discretization error in the calculation of the forcing terms was reduced. As a result, the numerical stability of the model is improved, while the maximum density ratio is still no more than 15. In addition, an index function was adopted to track the interface. Based on the model of He *et al.* [22], Lee *et al.* proposed a three-stage stable discretization scheme [23] and a second-order mixed difference scheme [24] to calculate the forcing terms so that a large density ratio can be reached. However, in their models [24,25], the total mass is not strictly conserved [26–28]. To improve stability at a low viscosity, the model of He *et al.* [22] was also extended to the multiple-relaxation-time (MRT) version [29].

In the aforementioned models [22,23,29] where an order function is used, the interface capturing equation, namely, the Chan-Hilliard (CH) equation [4], cannot be completely recovered [30,31]. To solve this problem, Zheng *et al.* [30]

---

[*] Corresponding author: shibc@hust.edu.cn

presented a LB model for interface capturing in which a spatial difference term of the distribution function was introduced. This term is used to produce the diffusion effect such that the CH equation can be recovered exactly. Utilizing this LB model for tracking the interface, they proposed a multiphase LB model and claimed that the model could tolerate a large density ratio [31]. However, the later work conducted by Fakhari and Rahimian [32] showed that the model [31] is limited to density-matched binary fluids and a MRT version of the multiphase LB model based on the work of Huang *et al.* [33] for interface tracking and the work of He *et al.* [22] for flow field was then proposed [32]. This MRT model is able to simulate multiphase flow with moderate density ratio and low viscosity, but some additional artifacts are included in the recovered interface equation, which affects the numerical accuracy of the model in capturing the interface (see Sec. III). Recently, similar to the work of Zheng *et al.* [30], to recover the CH equation, Zu and He [34] adopted a spatial difference term of the equilibrium distribution function instead of the distribution function. It is noted that the model for interface capturing becomes unstable as the relaxation time approaches 1.0 and also a prediction-correction step is needed to evaluate the pressure and velocity since they satisfy two implicit equations.

In this paper, we propose an alternative MRT LB model for incompressible multiphase fluid systems. The features of the present model are summarized as follows. First, a double-distribution-function model is utilized, in which one distribution function is used to solve the CH equation and the other is adopted to solve the Navier-Stokes (NS) equations. Second, different from the previous models [30,34], a time-derivative term is incorporated such that the CH equation can be recovered exactly. In addition, the MRT collision model is used instead of the single-relaxation-time (SRT) collision model to improve the numerical stability. Third, we introduce a modified pressure distribution function that results in the correct incompressible hydrodynamic equations and simultaneously the pressure and velocity can be obtained explicitly. Finally, the present model is capable of simulating low-viscosity or high-Reynolds-number flows and also guarantees the conservation of the total mass.

The rest of the present paper is organized as follows. In Sec. II, the phase-field theory is briefly introduced and then the present MRT model for multiphase flow systems is presented; the Chapman-Enskog analysis of the model is also conducted to match the target equations in the framework of phase-field theory. Numerical experiments to test the accuracy and stability of the present model are made in Secs. III and IV. As an application, the present model is also invoked to study the Rayleigh-Taylor instability at high Reynolds numbers. Finally, a brief summary is given in Sec. V.

II. PHASE-FIELD-BASED MRT LB MODEL FOR INCOMPRESSIBLE MULTIPHASE FLOWS

A. Phase-field theory

In the phase-field theory, the free energy of a multiphase system can be written as a function of the order parameter ϕ [4,35,36],

$$F(\phi) = \int_{\Omega} [\psi(\phi) + k|\nabla\phi|/2] d\Omega, \tag{1}$$

where Ω is the fluid domain occupied by the system, $\psi(\phi)$ denotes the bulk free-energy density, and $k|\nabla\phi|/2$ accounts for the surface energy with a positive coefficient k. If the system considered is a van der Waals fluid, then the bulk free energy has a double-well form [4]

$$\psi(\phi) = \beta(\phi - \phi_A)^2(\phi - \phi_B)^2, \tag{2}$$

where β is a constant relating to the interfacial thickness D and the surface tension σ by [4]

$$D = \frac{1}{|\phi_A - \phi_B|}\sqrt{\frac{8k}{\beta}} \tag{3}$$

and

$$\sigma = \frac{|\phi_A - \phi_B|^3}{6}\sqrt{2k\beta}. \tag{4}$$

Here ϕ_A and ϕ_B are constants that represent fluids A and B, respectively. With this bulk free energy, the chemical potential μ can be derived as

$$\begin{aligned}\mu &= \frac{\partial F(\phi)}{\partial\phi} = \frac{d\psi(\phi)}{d\phi} - k\nabla^2\phi \\ &= 4\beta(\phi - \phi_A)(\phi - \phi_B)\left(\phi - \frac{\phi_A + \phi_B}{2}\right) - k\nabla^2\phi. \end{aligned}\tag{5}$$

Solving the equation $\mu = 0$, one can obtain the one-dimensional interface profile at the equilibrium state (along the z direction),

$$\phi(z) = \frac{\phi_A + \phi_B}{2} + \frac{\phi_A - \phi_B}{2}\tanh\left(\frac{2z}{D}\right). \tag{6}$$

If we assume that the diffusion is driven by the chemical potential gradient, then the evolution of the order parameter should be governed by the CH equation [4,35,36]

$$\frac{\partial\phi}{\partial t} + \nabla\cdot\phi\mathbf{u} = \nabla\cdot M_\phi(\nabla\mu), \tag{7}$$

where M_ϕ is the mobility coefficient and $\mathbf{u}$ is the fluid velocity, and governed by the incompressible NS equations [4,34–38]

$$\nabla\cdot\mathbf{u} = 0, \tag{8a}$$

$$\rho\left(\frac{\partial\mathbf{u}}{\partial t} + \mathbf{u}\cdot\nabla\mathbf{u}\right) = -\nabla p + \nabla\cdot[\nu\rho(\nabla\mathbf{u} + \nabla\mathbf{u}^T)] + \mathbf{F}_s + \mathbf{G}, \tag{8b}$$

where p is the hydrodynamic pressure, ν is the kinematic viscosity, and $\mathbf{G}$ is the body force. Here the surface tension force takes the potential form $\mathbf{F}_s = \mu\nabla\phi$ [4,31].

B. The MRT LB model for the Cahn-Hilliard equation

The generalized evolution equation for the CH equation reads

$$h_i(\mathbf{x} + \mathbf{c}_i\delta t, t + \delta t) - h_i(\mathbf{x},t) = -\Lambda_{ij}^h[h_j(\mathbf{x},t) - h_j^{eq}(\mathbf{x},t)] + \delta_t R_i(\mathbf{x},t), \tag{9}$$

where $h_i(\mathbf{x},t)$ is the order distribution function with velocity $\mathbf{c}_i$ at position $\mathbf{x}$ and time t, Λ_{ij}^h is an element of the generalized collision matrix $\mathbf{\Lambda}^h$, and $R_i(\mathbf{x},t)$ is the source term. Here $h_i^{eq}(\mathbf{x},t)$ is the local equilibrium distribution function, which is defined as [32,33,39,40]

$$h_i^{eq}(\mathbf{x},t) = \begin{cases} \phi + (\omega_i - 1)\eta\mu, & i = 0 \\ \omega_i \eta\mu + \omega_i \frac{\mathbf{c}_i \cdot \phi\mathbf{u}}{c_s^2}, & i \neq 0, \end{cases}$$

where ω_i is the weighting coefficient, c_s is the speed of sound, and η is an adjustable parameter that controls the mobility. In the D2Q9 model, ω_i is given by $\omega_0 = 4/9$, $\omega_{1,\ldots,4} = 1/9$, $\omega_{5,\ldots,8} = 1/36$, $c_s = c/\sqrt{3}$, and $\mathbf{c}_i$ is defined as

$$\mathbf{c}_i = \begin{cases} (0,0)c, & i = 0 \\ (\cos[(i-1)\pi/2], \sin[(i-1)\pi/2])c, & i = 1,\ldots,4 \\ \sqrt{2}\{\cos[(i-5)\pi/2 + \pi/4], \sin[(i-5)\pi/2 + \pi/4]\}c, & i = 5,\ldots,8, \end{cases}$$

where $c = \delta_x/\delta_t$, with δ_x and δ_t representing the lattice spacing and time step, respectively. In this study, $c = \delta_x = \delta_t = 1.0$.

Based on the work of Lallemand and Luo [41], the collision operate $\mathbf{\Lambda}^h$ can be written as

$$\mathbf{\Lambda}^h = \mathbf{M}^{-1}\mathbf{S}^h\mathbf{M}, \tag{10}$$

where $\mathbf{M}$ is the transformation matrix

$$\mathbf{M} = \begin{pmatrix} 1 & 1 & 1 & 1 & 1 & 1 & 1 & 1 & 1 \\ -4 & -1 & -1 & -1 & -1 & 2 & 2 & 2 & 2 \\ 4 & -2 & -2 & -2 & -2 & 1 & 1 & 1 & 1 \\ 0 & 1 & 0 & -1 & 0 & 1 & -1 & -1 & 1 \\ 0 & -2 & 0 & 2 & 0 & 1 & -1 & -1 & 1 \\ 0 & 0 & 1 & 0 & -1 & 1 & 1 & -1 & -1 \\ 0 & 0 & -2 & 0 & 2 & 1 & 1 & -1 & -1 \\ 0 & 1 & -1 & 1 & -1 & 0 & 0 & 0 & 0 \\ 0 & 0 & 0 & 0 & 0 & 1 & -1 & 1 & -1 \end{pmatrix},$$

which can be used to project h_i and h_i^{eq} onto the moment space with $\mathbf{m}_h = \mathbf{Mh}$ and $\mathbf{m}_h^{eq} = \mathbf{Mh}^{eq}$, where $\mathbf{h} = (h_0,\ldots,h_8)^{\mathrm{T}}$ and $\mathbf{h}^{eq} = (h_0^{eq},\ldots,h_8^{eq})^{\mathrm{T}}$. Here $\mathbf{S}^h$ is a diagonal relaxation matrix

$$\mathbf{S}^h = \mathrm{diag}\left(s_0^h, s_1^h, s_2^h, s_3^h, s_4^h, s_5^h, s_6^h, s_7^h, s_8^h\right), \tag{11}$$

where $0 < s_i^h < 2$. We would like to point out that, if the s_i^h are equal to each other, the MRT model will reduce to the SRT model. The source term R_i in Eq. (9) is defined as

$$\mathbf{R} = \mathbf{M}^{-1}\left(\mathbf{I} - \frac{\mathbf{S}^h}{2}\right)\mathbf{M}\bar{\mathbf{R}}, \tag{12}$$

where $\mathbf{I}$ is the unit matrix, $\mathbf{R} = (R_0,\ldots,R_8)$, and $\bar{\mathbf{R}} = (\bar{R}_0,\ldots,\bar{R}_8)$ with [42]

$$\bar{R}_i = \frac{\omega_i \mathbf{c}_i \cdot \partial_t \phi\mathbf{u}}{c_s^2}. \tag{13}$$

Applying the Chapman-Enskog expansion to Eq. (9), we can derive the CH equation exactly with the mobility M_ϕ given by

$$M_\phi = \eta c_s^2(\tau_h - 0.5)\delta t, \tag{14}$$

where $\tau_h = 1/s_3^h = 1/s_5^h$ (see Appendix A). The order parameter in the present model is calculated as

$$\phi = \sum_i h_i \tag{15}$$

and the density is determined by the value of ϕ,

$$\rho = \frac{\phi - \phi_B}{\phi_A - \phi_B}(\rho_A - \rho_B) + \rho_B. \tag{16}$$

It should be noted that the MRT model for interface capturing proposed by Fakhari and Rahimian [32] is slightly different from our model in the evolution equation. In their model, the source term R_i is not included in Eq. (9), which leads to an artificial term in the recovered equation

$$\frac{\partial\phi}{\partial t} + \nabla\cdot(\phi\mathbf{u}) = \nabla\cdot M_\phi(\nabla\mu) + \left(1/s_3^h - 0.5\right)\delta t \nabla\cdot(\epsilon\partial_{t_1}\phi\mathbf{u}). \tag{17}$$

As can be clearly seen, the additional term of $O(\delta_t Ma)$ appears in the recovered equation, which will produce a larger error in the interface capturing compared to our model shown in Sec. III.

C. The MRT LB model for the incompressible Navier-Stokes equations

The starting point of the proposed model for the incompressible NS equations is the discrete Boltzmann equation with a generalized collision matrix Λ^f [22,25],

$$\frac{Df_i}{Dt} = \left(\frac{\partial}{\partial t} + \mathbf{c}_i\cdot\nabla\right)f_i = -\Lambda_{ij}^f\left(f_j - f_j^{eq}\right) + \frac{(\mathbf{c}_i - \mathbf{u})\cdot\mathbf{F}}{c_s^2}\Gamma_i(\mathbf{u}), \tag{18}$$

where f_i is the density distribution function, Λ_{ij}^f is an element of collision matrix $\mathbf{\Lambda}^f$, f_i^{eq} is the equilibrium distribution function

$$f_i^{eq} = \omega_i \rho + \rho s_i(\mathbf{u}),$$
$$s_i(\mathbf{u}) = \omega_i \left[\frac{\mathbf{c}_i \cdot \mathbf{u}}{c_s^2} + \frac{(\mathbf{c}_i \cdot \mathbf{u})^2}{2c_s^4} - \frac{\mathbf{u} \cdot \mathbf{u}}{2c_s^2} \right], \tag{19}$$

and $\Gamma_i(\mathbf{u}) = f_i^{eq}/\rho$. The total force $\mathbf{F}$ is defined as

$$\mathbf{F} = -\nabla\left(p - \rho c_s^2\right) + \mathbf{F}_s + \mathbf{F}_a + \mathbf{G}, \tag{20}$$

in which $\mathbf{F}_a = \frac{\rho_A - \rho_B}{\phi_A - \phi_B} \nabla \cdot (M_\phi \nabla \mu)\mathbf{u}$ is an interfacial force introduced by Li *et al.* [38].

Different from the previous works [22–25,32,38], we introduce a pressure distribution function

$$g_i = \begin{cases} f_i + (\frac{p}{c_s^2} - \rho)\Gamma(0) - \frac{p}{c_s^2}, & i = 0 \\ f_i + (\frac{p}{c_s^2} - \rho)\Gamma(0), & i \neq 0. \end{cases}$$

Taking the total derivative of the variable g_i, according to Eq. (18), the evolution equation of g_i can be written as

$$\frac{Dg_i}{Dt} = -\Lambda_{ij}^f \left(g_j - g_j^{eq}\right) + F_i, \tag{21}$$

where

$$g_i{}^{eq} = \begin{cases} \frac{p}{c_s^2}(\omega_i - 1) + \rho s_i(\mathbf{u}), & i = 0 \\ \frac{p}{c_s^2}\omega_i + \rho s_i(\mathbf{u}), & i \neq 0, \end{cases}$$

and

$$F_i = \frac{(\mathbf{c}_i - \mathbf{u})}{c_s^2} \cdot \{[\Gamma_i(\mathbf{u}) - \Gamma_i(0)]\nabla\left(\rho c_s^2\right)$$
$$+ (\mathbf{F}_s + \mathbf{F}_a + \mathbf{G})\Gamma_i(\mathbf{u})\}. \tag{22}$$

Note that the terms associated with $\mathbf{u} \cdot \nabla p$, which are of $O(Ma^3)$ for incompressible flows ($Ma \ll 1$), are dropped from Eq. (22). Integrating Eq. (21) from time t to $t + \delta_t$ and using the trapezoidal rule, one can obtain

$$g_i(\mathbf{x} + \mathbf{c}_i\delta_t, t + \delta_t) - g_i(\mathbf{x},t)$$
$$= \frac{\delta_t}{2}\left[-\Lambda_{ij}^f\left(g_j - g_j^{eq}\right) + F_i\right]$$
$$\Big|_{(\mathbf{x}+\mathbf{c}_i\delta_t, t+\delta_t)} + \frac{\delta_t}{2}\left[-\Lambda_{ij}^f\left(g_j - g_j^{eq}\right) + F_i\right]\Big|_{(\mathbf{x},t)}. \tag{23}$$

Here the evolution equation for g_i is implicit, as shown in Eq. (23). To remove this implicitness, we introduce a modified particle distribution function

$$\bar{g}_i = g_i - \frac{\delta_t}{2}\left[-\Lambda_{ij}^f\left(g_j - g_j^{eq}\right) + F_i\right]. \tag{24}$$

Then Eq. (23) can be recast as

$$\bar{g}_i(\mathbf{x} + \mathbf{c}_i\delta_t, t + \delta_t) = g_i(\mathbf{x},t) + \frac{\delta_t}{2}\left\{-\Lambda_{ij}^f\left[g_j(\mathbf{x},t) - g_j^{eq}(\mathbf{x},t)\right]\right.$$
$$\left. + F_i(\mathbf{x},t)\right\}. \tag{25}$$

Similar to Eq. (10), $\mathbf{\Lambda}^f$ can be expressed as [41,43]

$$\mathbf{\Lambda}^f = \mathbf{M}^{-1}\mathbf{S}^f\mathbf{M}, \tag{26}$$

where $\mathbf{S}^f = \mathrm{diag}(s_0^f, s_1^f, s_2^f, s_3^f, s_4^f, s_5^f, s_6^f, s_7^f, s_8^f)$, and then we can rewrite Eq. (25) in the vector form

$$\bar{\mathbf{g}}(\mathbf{x} + \mathbf{c}_i\delta_t, t + \delta_t)$$
$$= \mathbf{M}^{-1}\left[\left(\mathbf{I} - \frac{\delta_t}{2}\mathbf{S}^f\right)\mathbf{m}_g + \frac{\delta_t}{2}\mathbf{S}^f\mathbf{m}_g^{eq} + \frac{\delta_t}{2}\mathbf{M}\bar{\mathbf{F}}\right], \tag{27}$$

where $\bar{\mathbf{g}}$ and $\bar{\mathbf{F}}$ are the 9-tuple vectors of the distribution functions $\bar{g}_i$ and F_i, respectively, $\mathbf{m}_g = \mathbf{M}\mathbf{g}$, and $\mathbf{m}_g^{eq} = \mathbf{M}\mathbf{g}^{eq}$ with $\mathbf{g} = (g_0, \ldots, g_8)^{\mathrm{T}}$ and $\mathbf{g}^{eq} = (g_0^{eq}, \ldots, g_8^{eq})^{\mathrm{T}}$. Based on the definition of $\bar{g}_i$, given by Eq. (24), one can easily derive

$$\mathbf{m}_g = \left(\mathbf{I} + \frac{\delta_t}{2}\mathbf{S}^f\right)^{-1}\left[\bar{\mathbf{m}}_g + \frac{\delta_t}{2}\mathbf{S}^f\mathbf{m}_g^{eq} + \frac{\delta_t}{2}\mathbf{M}\bar{\mathbf{F}}\right], \tag{28}$$

where $\bar{\mathbf{m}}_g = \mathbf{M}\bar{\mathbf{g}}$ with $\bar{\mathbf{g}} = (\bar{g}_0, \ldots, \bar{g}_8)^{\mathrm{T}}$. Substituting Eq. (28) into Eq. (27), with some matrix manipulations we can obtain the evolution equation for $\bar{g}_i$ in an explicit scheme

$$\bar{g}_i(\mathbf{x} + \mathbf{c}_i\delta_t, t + \delta_t) - \bar{g}_i(\mathbf{x},t)$$
$$= -[\mathbf{M}^{-1}\mathbf{S}^g\mathbf{M}]_{ij}\left[\bar{g}_j(\mathbf{x},t) - g_j^{eq}(\mathbf{x},t)\right]$$
$$+ \delta_t\left[\mathbf{M}^{-1}\left(\mathbf{I} - \frac{\mathbf{S}^g}{2}\right)\mathbf{M}\right]_{ij} F_j(\mathbf{x},t), \tag{29}$$

where $\mathbf{S}^g = \mathrm{diag}(s_0^g, s_1^g, s_2^g, s_3^g, s_4^g, s_5^g, s_6^g, s_7^g, s_8^g)$, $s_i^g = \frac{2\delta_t s_i^f}{2+\delta_t s_i^f}$ for all i, and the MRT model also reduces to the SRT version if all the elements of $\mathbf{S}^g$ are identical to each other. By taking the first-order moment of $\bar{g}_i$, the fluid velocity can be obtained

$$\mathbf{u} = \left[\sum_i \mathbf{c}_i\bar{g}_i + 0.5\delta_t(\mathbf{F}_s + \mathbf{G})\right] \Big/$$
$$[\rho - 0.5\delta_t(\rho_A - \rho_B)\nabla \cdot M_\phi\nabla\mu/(\phi_A - \phi_B)]. \tag{30}$$

As shown in Appendix B, the pressure can be calculated as

$$p = \frac{c_s^2}{1 - \omega_0}\left[\sum_{i\neq 0}\bar{g}_i + \frac{\delta_t}{2}\mathbf{u} \cdot \nabla\rho + \rho s_0(\mathbf{u})\right] \tag{31}$$

and the kinematic viscosity is determined by

$$\nu = c_s^2(\tau_g - 0.5)\delta_t, \tag{32}$$

where $\tau_g = 1/s_7^g = 1/s_8^g$. Note that the fluid velocity and pressure in our model can be computed explicitly [see Eqs. (30) and (31)], while a prediction-correction step is needed to evaluate them in the previous model [34]. In addition, the present model can also recover the incompressible hydrodynamic equations exactly (see Appendix B for details).

III. NUMERICAL TESTS FOR THE INTERFACE-CAPTURING LB MODEL

In this section, we validate the proposed LB model for interface capturing by using three benchmark tests: Zalesak's disk rotation [44], a single vortex [45], and a deformation field [46]. In these validations, Eq. (9) is only used since the velocity field has been prespecified. To quantitatively describe the accuracy of the present model and compare with the existing LB models [30,32,34], the following relative error

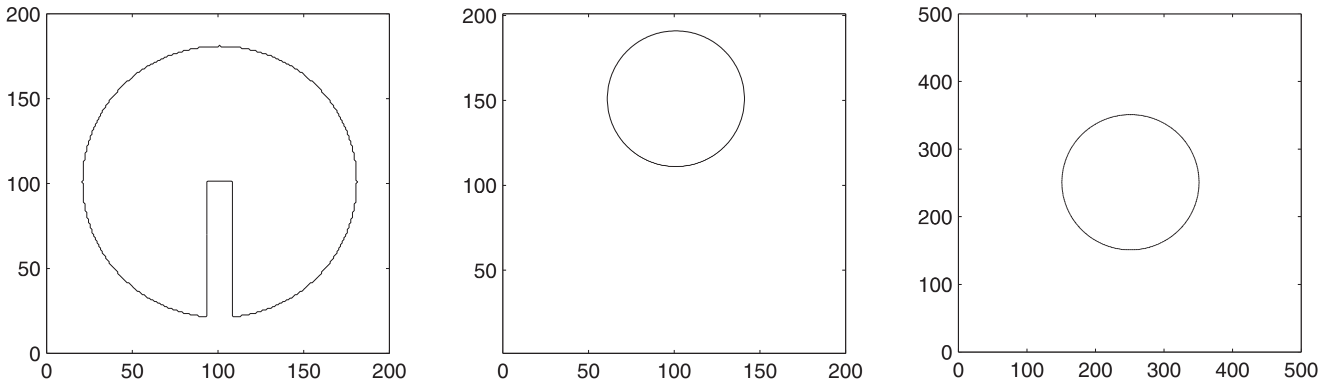

(a) (b) (c)

FIG. 1. Initial setup for three tests: (a) Zalesak's disk rotation, (b) a single vortex, and (c) a deformation field.

is used [47]:

$$E_\phi = \frac{\sum\limits_{\mathbf{x}} |\phi(\mathbf{x},T) - \phi(\mathbf{x},0)|}{\sum\limits_{\mathbf{x}} |\phi(\mathbf{x},0)|}, \tag{33}$$

where $\phi(\mathbf{x},T)$ is the computational result of order parameter after a periodic time T and $\phi(\mathbf{x},0)$ is the initial solution. In the present study, the explicit difference scheme [39] $\partial_t \chi(\mathbf{x},t) = [\chi(\mathbf{x},t) - \chi(\mathbf{x},t-\delta_t)]/\delta_t$ is used for computing the time derivative in Eq. (13) and the second-order isotropic central schemes [27]

$$\nabla \chi(\mathbf{x},t) = \sum_{i\neq 0} \frac{\omega_i \mathbf{c}_i \chi(\mathbf{x}+\mathbf{c}_i\delta_t,t)}{c_s^2 \delta_t}, \tag{34a}$$

$$\nabla \chi^2(\mathbf{x},t) = \sum_{i\neq 0} \frac{2\omega_i [\chi(\mathbf{x}+\mathbf{c}_i\delta_t,t) - \chi(\mathbf{x},t)]}{c_s^2 \delta_t^2} \tag{34b}$$

are adopted to discretize the spatial gradients since the global mass conservation can be guaranteed [28]. Here χ is an arbitrary function.

A. Zalesak's disk rotation

Zalesak's disk is a widely used case to test basic features of an interface capturing model. In this test the disk with a slot is initially placed at the center of a 200×200 square computation domain, as illustrated in Fig. 1(a). The disk radius and the slot width are set as 80 and 16 in lattice units, respectively. The rotation of the disk is driven by a vortex flow with the velocity (u,v),

$$u = -w(y - 0.5d), \quad v = w(x - 0.5d), \tag{35}$$

where $d = 200$ and w is a constant angular velocity. Here we set $w = U_0\pi/d$ such that the disk will return to its initial location after one period $T = 2d/U_0$. In our simulations, some other physical parameters are set as $D = 2.0$, $\sigma = 0.04$, and $\phi_A = -\phi_B = 1.0$. The order parameter is initialized by ϕ_A inside the disk and ϕ_B elsewhere. The relaxation times s_3^h and s_5^h are chosen as $\frac{4}{3}$, which corresponds to the relaxation time of 0.75 taken in Zu and He's model [34]. Considering the components of the equilibrium in moment space, we fix $s_0^h = s_7^h = s_8^h = 1.0$ as usual, $s_1^h = s_2^h$, and $s_4^h = s_6^h$. The relaxation times s_1^h $(= s_2^h)$ and s_4^h $(= s_6^h)$ can be freely adjusted to improve the stability and accuracy of the MRT model. In this test, s_1^h ranging from 0.8 to 1.3 and s_4^h in the wide scope of $0.6 \leqslant s_4^h \leqslant 1.4$ can give good results. As one case, we set $s_1^h = s_2^h = s_4^h = s_6^h = 1.3$. To simplify the description, the dimensionless Péclet number (Pe) is introduced and is defined as $\mathrm{Pe} = U_0 D / M_\phi \beta(\phi_A - \phi_B)^2$ [34]. Unless otherwise specified, the periodic boundary conditions are applied at all boundaries.

We first present a comprehensive comparison among different LB models. Figure 2 shows the interface patterns after one period at $\mathrm{Pe} = 200$ and $U_0 = 0.025$. Note that the interface is displayed by the contour level of $\phi = 0$. We can clearly see that the results by the model of Zheng

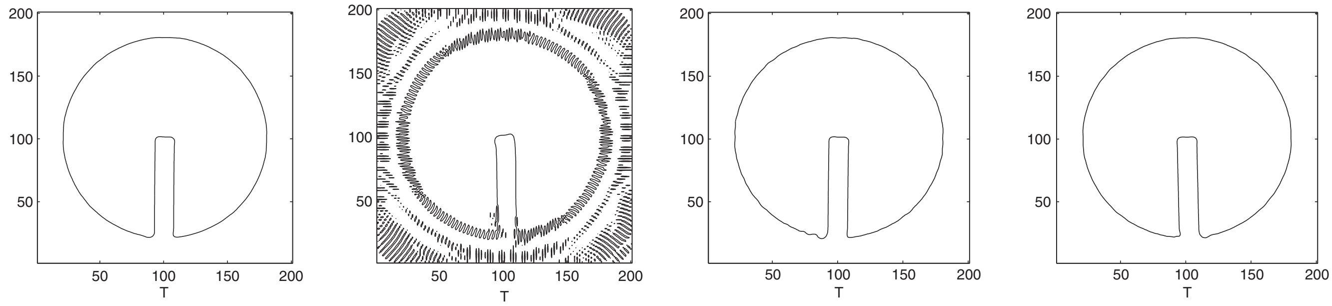

(a) (b) (c) (d)

FIG. 2. Results of Zalesak's disk test after one period at $\mathrm{Pe} = 200$ and $U = 0.025$ for (a) the present model, (b) the model of Zheng *et al.* [30], (c) Fakhari and Rahimian's model [32], and (d) Zu and He's model [34].

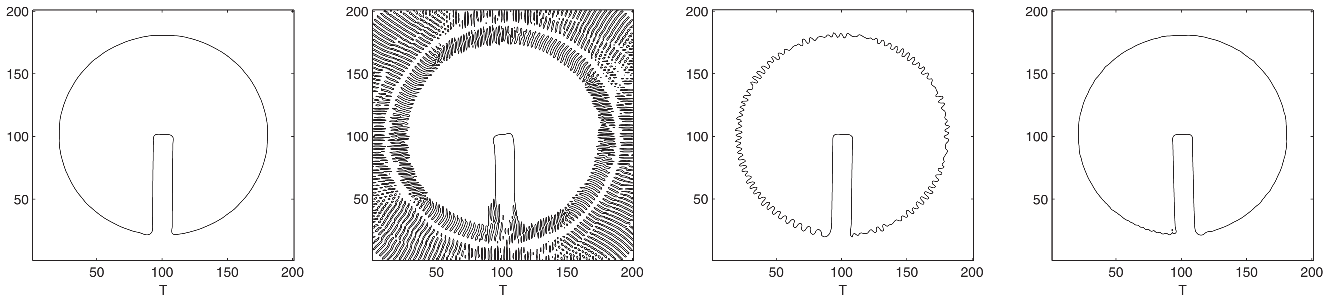

(a) (b) (c) (d)

FIG. 3. Results of Zalesak's disk test after one period at Pe = 200 and $U = 0.04$ for (a) the present model, (b) model B [30], (c) model C [32], and (d) model D [34].

et al. [30] (labeled as model B) are unstable, which not only produce quantities of sawteeth along the edge of the disk, but also present many unphysical disturbances around the square computational domain. In contrast, the other three models give a more stable interface. Nonetheless, a small distortion near the corner of the slot is observed in the results of Fakhari and Rahimian's model [32] (labeled as model C) and the results by Zu and He's model [34] (labeled as model D) are slightly asymmetric. As mentioned above, the recovered equation by model C contains an additional term, which is of $O(\delta_t Ma)$. To see the effect of the term more clearly, we performed the simulations in which Pe is kept at 200, but U_0 is increased to 0.04. As shown in Fig. 3, we can observe that there exist some obvious jagged shapes in the vicinity of the interface, which indeed produce a larger error than the last situation. Model B is still worst in tracking the interface and the results of model D are slightly twisted at the corner of the slot, while our model generates relatively accurate results. To show the advantage of our present model, we further conducted numerical tests at a larger Péclet number. Figure 4 shows the results at Pe = 700 and $U_0 = 0.025$. It is obvious from Fig. 4 that the previous models induce some diffusion around the edge of the disk and also quantities of jetsam. On the contrary, our present model can still obtain a stable and accurate interface. To give a quantitative comparison among these models, the relative errors E_ϕ after one period were computed and are listed in Table I. It can be seen that our model is much more accurate than the other three models in capturing the interface, especially at a larger Péclet number. Actually, obtaining an accurate order parameter is very important in that the density field is determined by the value of the order parameter.

Finally, to show some advantages of the present MRT model over the SRT version, a comparison between them is conducted with the above two cases. The SRT model is derived when all the relaxation parameters in $\mathbf{S}^h$ are equal. Here we set all s_i^h as $\frac{4}{3}$. Figure 5 shows the disk interface at time T by the SRT model. It can be seen that the SRT model can obtain a stable interface at a low Péclet number of 200. However, when the Péclet number is increased to 700, the results of the SRT model become unstable, which produce many disturbances around the edge of the disk. In contrast, the MRT model can still obtain good results [see Fig. 4(a)], which suggests that the MRT model is much more stable and accurate than the SRT model in capturing the interface.

B. Single vortex

As shown above, Zalesak's disk test does not cause large topological changes in which the shape of the interface remains unchanged during the rotation process. In order to test the capacity of the present MRT model in capturing a more deformed and stretched interface, the time-reversed single-vortex test is also considered. This test poses some challenges as the velocity field is time dependent and strongly nonlinear,

$$\begin{aligned} u &= U_0 \sin^2\frac{\pi x}{d}\sin\frac{2\pi y}{d}\cos\frac{\pi t}{T}, \\ v &= -U_0 \sin\frac{2\pi x}{d}\sin^2\frac{\pi y}{d}\cos\frac{\pi t}{T}, \end{aligned} \tag{36}$$

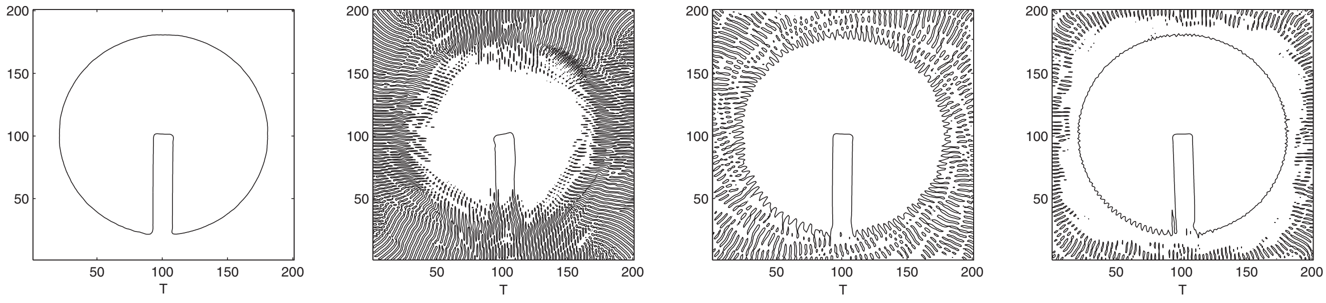

(a) (b) (c) (d)

FIG. 4. Results of Zalesak's disk test after one period at Pe = 700 and $U = 0.025$ for (a) the present model, (b) model B, (c) model C, and (d) model D.

TABLE I. Relative errors of Zalesak's disk test.

Pe	U_0	Present model	Model B	Model C	Model D
200	0.025	2.75×10^{-2}	5.07×10^{-1}	2.95×10^{-2}	3.12×10^{-2}
200	0.04	2.76×10^{-2}	7.96×10^{-1}	8.44×10^{-2}	3.28×10^{-2}
700	0.025	4.93×10^{-2}	1.58	6.3×10^{-1}	4.03×10^{-1}

where t is the evolution time scaled by d/U_0. The initial setup is shown in Fig. 1(b), where the computational grid is 200×200 and the disk has a radius of 40 centered at (100,150). The simulated parameters σ, D, ϕ_A, ϕ_B, and $\mathbf{S}^h$ are the same as those in the previous test. The order parameter is set equal to ϕ_A inside the disk and ϕ_B outside the disk, respectively, and a period T is set equal to 6. Theoretically, the disk's interface will be stretched progressively into a thin filament that spirals towards the vortex center until undergoing the largest deformation at time $T/2$. Then, if the velocity field is reversed in time, the disk will return to its initial position at time T. We tested this problem with different models and present the results in Fig. 6, where $\mathrm{Pe} = 500$ and $U_0 = 0.04$. We can see that in the results of the present model, the disk can return to its original position without any distortion after one period. Models C and D can also give accurate results, while some serious distortions around the disk can be observed in the results of model B. As expected, if we increase the velocity U_0, model C would have a larger error. To confirm this statement, we performed the simulations at $\mathrm{Pe} = 500$ and a larger velocity $U_0 = 0.08$. As seen from Fig. 7, we not only observe that the interface of the disk obtained by model C has some distortions, but also find that some unphysical disturbances appear both inside and outside the disk. Similar unphysical phenomena are also observed in the results of models B and D. On the contrary, the present model can give the accurate results. In order to test the ability of our model for the case with large Pélect number, we also carried out some simulations at $\mathrm{Pe} = 1500$. From Fig. 8 it can be clearly seen that the present model can still obtain a stable and accurate interface while the other three models produce some unphysical disturbances. The relative errors E_ϕ were calculated to give a quantitative comparison among the four models and are summarized in Table II. It can be found that the present model generates a smaller error than the other three models at a large Péclet number or a large velocity.

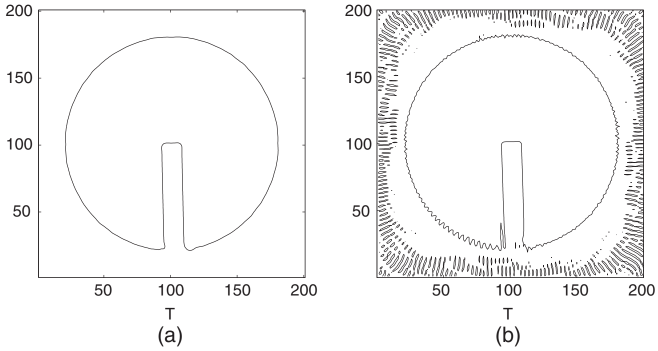

(a) (b)

FIG. 5. Results of Zalesak's disk test by the SRT model at (a) $\mathrm{Pe} = 200$ and $U = 0.025$ and (b) $\mathrm{Pe} = 700$ and $U = 0.025$.

C. Deformation field

The above two tests have shown the advantage of the present model in interface capturing. To further present the capacity of the present model, here we also apply it to study the problem of deformation field, which is considered one of the most stringent benchmarking problems including complex evolution of the interface [46]. Initially, a circular body with a radius of 100 is placed in the middle of the computational domain 500×500, as illustrated in Fig. 1(c). The velocity (u,v) is given by

$$\begin{aligned} u &= -U_0 \sin\left[n\pi\left(\frac{x}{d}+0.5\right)\right]\sin\left[n\pi\left(\frac{y}{d}+0.5\right)\right]\cos\frac{\pi t}{T},\\ v &= -U_0 \cos\left[n\pi\left(\frac{x}{d}+0.5\right)\right]\cos\left[n\pi\left(\frac{y}{d}+0.5\right)\right]\cos\frac{\pi t}{T}, \end{aligned} \tag{37}$$

where t is the scaled time by d/U_0 and n is the number of vortices. In our simulations, $U_0 = 0.025$, $n = 4$, $T = 1.25$, and the Péclet number is fixed at 200. The rest of the parameters are set as those in Zalesak's disk test. Figure 9 shows the evolution of the interface in one period T. During the first half period, the circular body is continuously entrained by the vortices and a very thin filamentary structure is formed at time $T/2$, while in the second half period, the thin filament moves back and returns to the initial configuration at time T. We clearly see from Fig. 9 that the symmetry of the interface is well retained and the final profile of the interface at time T is almost the same as the initial state. The relative error E_ϕ is approximately 1.22×10^{-2}, which has the same order as those in the previous two tests.

IV. NUMERICAL TESTS FOR THE MRT LB MODEL FOR MULTIPHASE FLOWS

A. Static droplet test

A basic static droplet test is first performed to validate the present model for multiphase flows. Initially, the droplet with $R = 25$ is placed at the center of a 100×100 lattice domain and the periodic boundary condition is applied at all boundaries. In our simulations, some physical parameters are fixed as $\rho_A = 1.0$, $\rho_B = 100.0$, $D = 5.0$, $\sigma = 0.001$, $\phi_A = -\phi_B = -1.0$, and $s_3^h = s_5^h = 1.25$; the other relaxation parameters in $\mathbf{S}^h$ are chosen to be the same as those in Sec. III. Note that s_0^g, s_3^g, and s_5^g have no influence on the deriving of the NS equations. For simplicity, the relation $s_0^g = s_3^g = s_5^g = 1.0$ is used [29]. Here s_7^g and s_8^g are set equal to 1.88, which can be used to derive a low kinematic viscosity $\nu = 0.01$. The other relaxation factors in $\mathbf{S}^g$ are chosen as $s_1^g = s_2^g = 1.0$ and $s_4^g = s_6^g = 1.7$ [25]. The initial interface profile is given by

$$\phi(x,y) = \frac{\phi_B+\phi_A}{2} + \frac{\phi_B-\phi_A}{2} \times \tanh\left(2\frac{R-\sqrt{(x-x_c)^2+(y-y_c)^2}}{D}\right), \tag{38}$$

where (x_c,y_c) is the coordinate of droplet center. Based on Eq. (16), one can derive the corresponding initial density

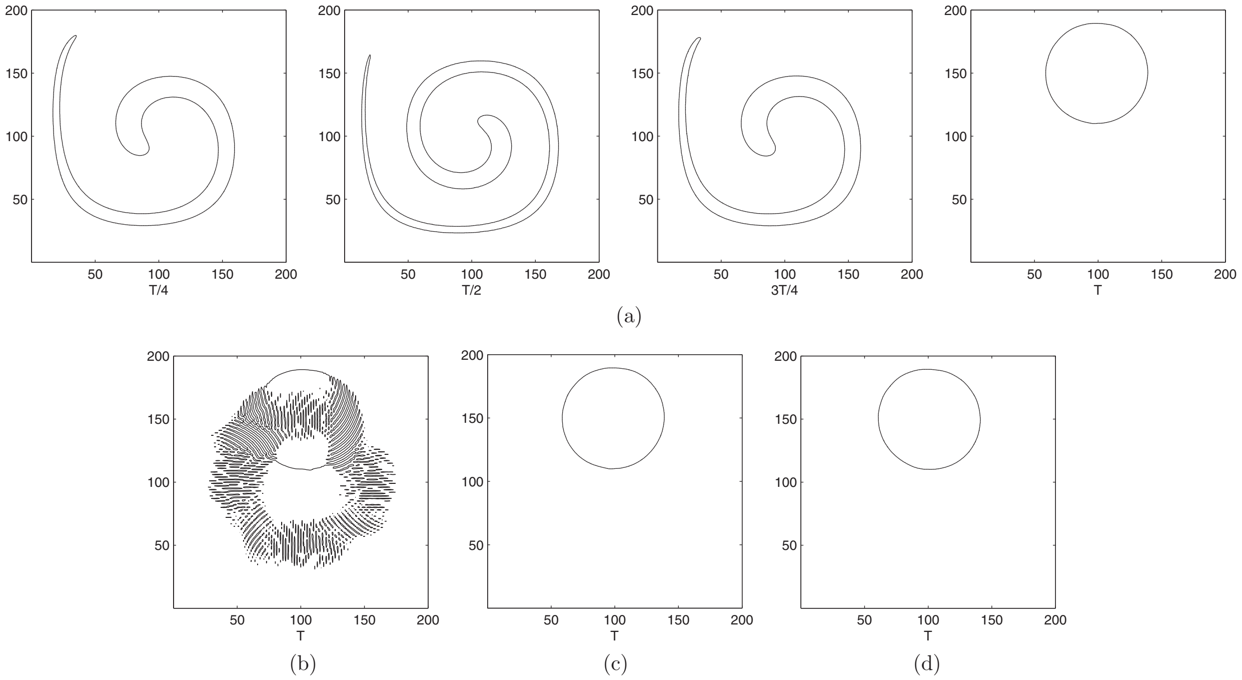

(a)

(b)

(c)

(d)

FIG. 6. Results of the single-vortex test at Pe = 500 and $U = 0.04$ for (a) the present model, (b) model B, (c) model C, and (d) model D.

profile

$$\rho(x,y) = \frac{\rho_B+\rho_A}{2} + \frac{\rho_B-\rho_A}{2} \times \tanh\left(2\frac{R-\sqrt{(x-x_c)^2+(y-y_c)^2}}{D}\right). \quad (39)$$

Figure 10(a) shows the density distribution as a function of the distance from the droplet center with three values of mobility $M_\phi = 0.01, 0.1, 1.0$. It can be clearly seen that the density profiles for three cases retain the original shape, except for a slight deviation at the interface for $M_\phi = 1.0$. This minor deviation is induced by the increasing diffusion effect as the value of mobility becomes large [34]. The pressure distribution across the domain center for $M_\phi = 0.01$ is presented in Fig. 10(b), where the pressure is calculated by $P = p - k\phi\nabla^2\phi - k|\nabla\phi|^2/2 + p_0$ and $p_0 = \phi\partial_\phi\psi - \psi$ is the equation of state [32,34]; P_A and P_B are the pressures of fluids A and B. According to the Laplace law, we can get the ratio between the surface tension computed by our model and the one given in Eq. (4), $\sigma_{\rm MRT}/\sigma = R(P_B - P_A)/\sigma = 0.965$, which suggests that the Laplace law is well satisfied.

We next consider the spurious velocity produced by the present model. The spurious velocity is a common concerning problem in two-phase flows [27,48] and cannot be completely removed [27]. However, it may benefit from the extra flexibility to reduce the spurious velocity if the MRT model is adopted in the collision process [48]. In Fig. 10(c), the velocity fields derived by both the present MRT model and the SRT version are shown. Here the SRT model is derived when the SRT collision scheme is used for both the CH equation and the NS equations. It can be clearly seen from Fig. 10(c) that spurious velocities by the SRT model appear around the edge of the droplet, while they can be reduced to some extent by the MRT model. The maximum magnitudes of the spurious velocity generated by the MRT model and the SRT version are 7.1×10^{-8} and 7.8×10^{-6}, respectively. In addition to weakening the spurious current, the MRT model is also able to reduce the large fluctuation of the maximal kinetic energy $E_{\max} = (\rho|\mathbf{u}|^2/2)_{\max}$ at early times, as shown in Fig. 10(d). In the

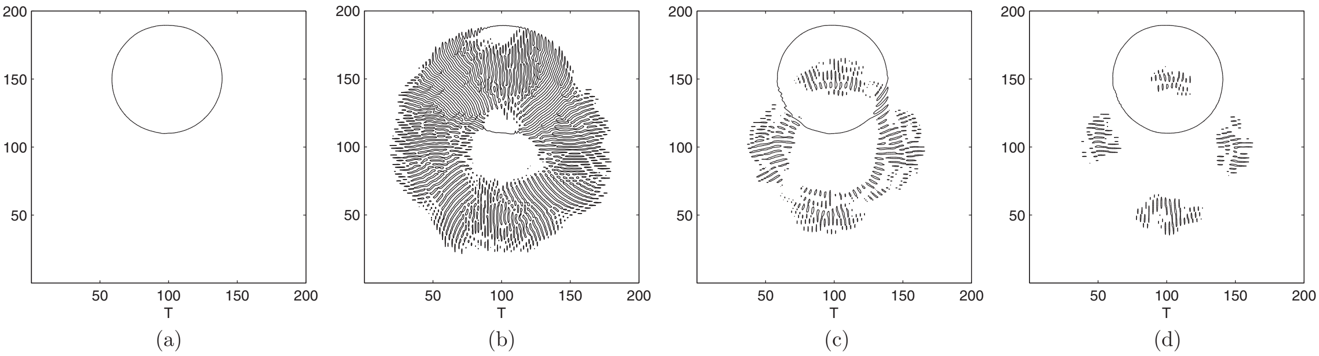

(a) (b) (c) (d)

FIG. 7. Results of the single-vortex test at Pe = 500 and $U = 0.08$ for (a) the present model, (b) model B, (c) model C, and (d) model D.

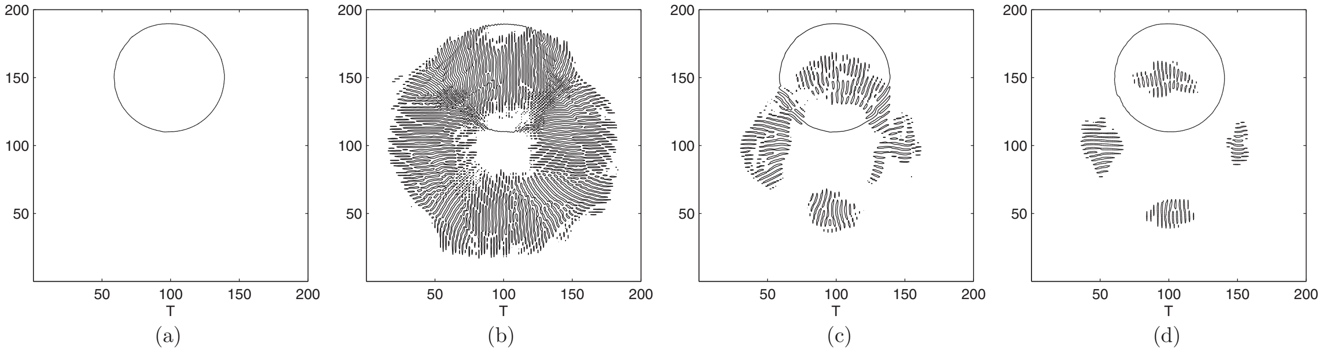

FIG. 8. Results of the single-vortex test at Pe = 1500 and $U = 0.04$ for (a) the present model, (b) model B, (c) model C, and (d) model D.

MRT model $E_{\max}$ varies from 10^{-13} to 10^{-11} at the initial stage, whereas it suffers from a large fluctuation ranging from 10^{-12} to 10^{-4} in the SRT model.

B. Rayleigh-Taylor instability

To demonstrate the capacity of the present model in the study of the high-Reynolds-number two-phase flows, we conducted some simulations of Rayleigh-Taylor instability (RTI) [49] at high Reynolds numbers. Rayleigh-Taylor instability is a fundamental interfacial instability that will occur when a heavier fluid is accelerated against a lighter one in the presence of a slight perturbation at the interface. This instability plays a significant role in extensive areas such as astrophysics [50] and confinement fusion [51]. Due to its wide and important applications, the RTI has been extensively studied by using experimental measurements [52], theoretical analysis [53–56], and as well as numerical approaches [22,34,37,38,57–61]. However, the Reynolds number considered in the previous works is relatively low and the late-time quantitative description of the immiscible RTI at high Reynolds numbers is still lacking. To fill this gap, the immiscible RTI at high Reynolds numbers is studied by the present model.

The physical system we consider here is a domain of $[0,d] \times [0,4d]$, which consists of two layers of fluids with a heavy fluid at the top and a light one at the bottom. The initial interface is $h = 2d + 0.05d\cos(2\pi x/\lambda)$, where λ is the wavelength. To be smoothed across the interface, the initial order profile is set as $\phi(x,y) = \tanh 2(y-h)/D$. The dimensionless Reynolds number and the Atwood number (A) characterizing RTI are defined respectively as [62]

$$\mathrm{Re} = \lambda\sqrt{Ag\lambda/(1+A)}/\nu, \quad A = (\rho_l - \rho_g)/(\rho_l + \rho_g). \tag{40}$$

In our simulations, the physical parameters are fixed as $d = \lambda = 256$, $\sqrt{g\lambda} = 0.04$, $A = 0.1$, Pe = 40, $D = 4.0$, and $\sigma = 5.0 \times 10^{-5}$ and the relaxation parameters in $\mathbf{S}^h$ and $\mathbf{S}^g$ are given as those in the above static droplet tests except for s_7^g and s_8^g; s_7^g and s_8^g are adjustable according to the value of the Reynolds number. The boundary conditions adopted are those in Ref. [22]. The computational mesh 256×1024 is used since it already gives grid-independent results. The detailed grid-independent test is deferred to Appendix C. Figure 11 depicts the evolution of the instability at four different values of Re. From Fig. 11 we can observe the significantly distinct behaviors of instability at different values of Re. At high Re, the spike of the heavy fluid first falls down and gradually rolls up, forming into two counterrotating vortices. Then these two vortices continue to grow, which results in a pair of secondary vortices at the tails of the roll-ups. Finally, the interface undergoes a chaotic breakup, which induces the formation of an abundance of small dissociative droplets in the system. In contrast, at low Re the spike of the heavy fluid falls down and the bubble of the light fluid rises up slowly and no vortices are observed in the whole process as the shear layer between the bubble and spike is stabilized due to the larger viscosity effect. We also conducted a quantitative study of the Reynolds number effect. Figures 12(a) and 12(b) present the evolution of the normalized bubble amplitude and velocity with nondimensional time. The normalized bubble velocity is commonly referred to as the bubble Froude number, which is defined as $\mathrm{Fr}_b = u_b/\sqrt{Ag\lambda/(1+A)}$ [63]. For the high-Re case, the RTI undergoes a number of stages, including linear growth, terminal velocity, reacceleration, and chaotic development. At the linear stage ($t \leqslant 1$), the amplitude has a growth with an exponential form [52] and the growth rate γ is given by the well-known linear theory [52,53]

$$\gamma = \sqrt{Agk - \sigma k^3/(\rho_l + \rho_g)}, \tag{41}$$

where $k = 2\pi/\lambda$ is the wave number. It should be noted that the above formula is the theoretical result of inviscid fluids subjected to surface tension. Combining the effect of viscous force, Menikoff *et al.* [54] proposed the lower and upper bounds to the growth rate, which are the solutions of the quartic and quadratic equations (see Appendix D for details). Figure 14 shows the growth rates at various values of Re. It is seen that the present model can give accurate predictions of the growth rate, which are located in the region between the lower and upper bounds. At the second stage, the bubble evolves with a constant terminal velocity that is sustained for $1 \leqslant t \leqslant 2.5$. The classic potential flow model [55] analytically predicts constant bubble and spike velocities

TABLE II. Relative errors of the single-vortex test.

Pe	U_0	Present model	Model B	Model C	Model D
500	0.04	2.74×10^{-2}	4.67×10^{-1}	2.72×10^{-2}	2.72×10^{-2}
500	0.08	2.81×10^{-2}	8.4×10^{-1}	2.14×10^{-1}	1.32×10^{-1}
1500	0.04	3.55×10^{-2}	1.22	2.58×10^{-1}	1.59×10^{-1}

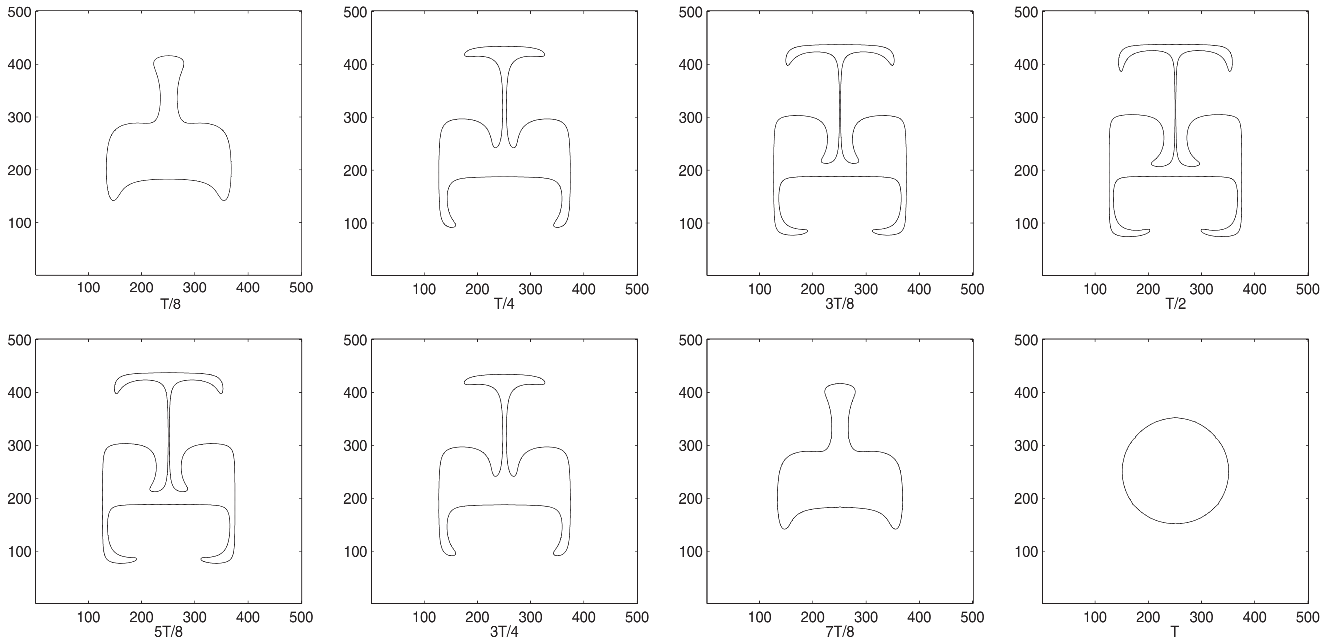

T/8 T/4 3T/8 T/2

5T/8 3T/4 7T/8 T

FIG. 9. Results of the deformation field test at Pe = 200 and $U = 0.04$ for the present model.

$u_{b,s} = \sqrt{2Ag/3k(1 \pm A)}$, yielding a bubble Froude number of 0.325 and a spike Froude number of 0.365, respectively. We compared the simulated results Fr_b and Fr_s with these theoretical values in Figs. 12(b) and 13(b). It can be found that good agreement between them can be achieved. For $2.5 \leqslant t \leqslant 3.5$, however, the vortical interactions gradually increase and begin to affect the velocities at the tips of the bubble and spike. Due to this increasing vortical effect, the bubble and spike are accelerated such that the velocities in this region diverge from the solutions to a potential flow problem. This process is termed reacceleration and was first identified by Glimm *et al.* [64] and further verified by Ramaprabhu *et al.* [65]. The reacceleration cannot go on continuously. After $t \geqslant 3.5$, the bubble Froude number becomes unstable and begins to fluctuate with the time, suggesting that the evolution has transformed to the chaotic stage. To show the nature of the growth at this stage, we present the normalized bubble acceleration $a/2Ag$ in Fig. 15(a), in which the smaller wavelength $\lambda = 128$ case was chosen to make the simulation last longer. As can be seen from Fig. 15(a), the normalized acceleration at late time fluctuates around a constant value of 0.07, resulting in a stationary average acceleration. Therefore, the bubble front at late time has a quadratic growth as $h_b = \alpha A g t^2$, where the coefficient α is 0.07. The quadratic growth at late time was also observed in previous work [62]. With this value, the bubble Froude number at late time fluctuates around the trajectories having the corresponding slope of 0.15, as shown in Fig. 15(b). For the low-Re case, some late growth stages, such as reacceleration and chaotic development, maybe no longer be attained. For instance, at Re = 30, the late-time flow at the tip of bubble is approximately described by the potential flow approach, as the bubble Froude number during this stage approaches a constant value [see Fig. 12(b)]. Both the chaotic stage and reacceleration are no longer observed. It is also noted that the terminal bubble Froude number is below the theoretical value of 0.325. That is because the viscosity effect becomes important when the Reynolds number is small enough. Banerjee *et al.* [56] recently realized this effect and modified the terminal bubble velocity including viscous effects and vorticity w_0 as

$$\mathrm{Fr}_b = \left(\sqrt{\frac{2Ag}{3(1+A)k} + \frac{1-A}{1+A}\frac{w_0^2}{4k^2} + \frac{4}{9}k^2\nu^2} - \frac{2}{3}k\nu\right) \Bigg/ \times \sqrt{\frac{Ag\lambda}{1+A}}. \tag{42}$$

Based on Eq. (42), the terminal Fr_b for Re = 30 is 0.248, which is slightly smaller than the 0.26 given by the present model.

We also carried out the simulation to give a comparison with the experiment of immiscible RTI by Waddell *et al.* [52]. In their experiment, the Atwood number was 0.336 and the Reynolds number was approximately 10 000 based on the definition in Eq. (40). The two immiscible fluids in a 121-mm-wide tank were accelerated by 1.34**g** with an initial wavelength of 35 mm. Figure 16 depicts a sequence of the interface patterns obtained by the present model. It is found that the behaviors of the interface are very close to experimental images presented in Fig. 6 of Ref. [52]. The main structures such as the roll-ups and the late-time chaos in the experiment are also observed in our simulations. We further present the bubble and spike amplitudes as functions of time in Fig. 17, where the marked points were taken from experimental measurements. As can be seen from Fig. 17, the simulation results are in good agreement with the experimental data.

V. SUMMARY

In this paper, a MRT LB model based on the phase-field theory was developed for incompressible multiphase flow systems. In this model, two distribution functions are utilized to solve the CH equation and the incompressible NS equations. The Champan-Enskog analysis shows that both

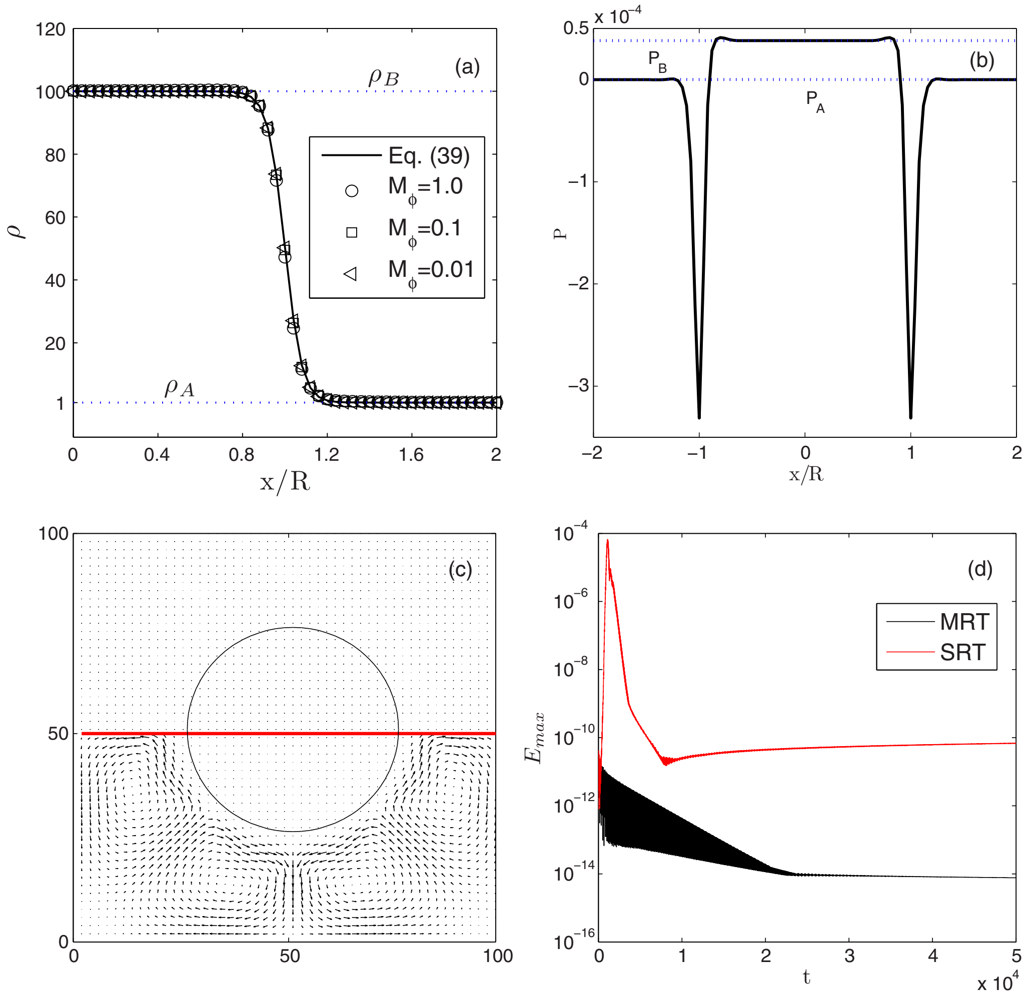

FIG. 10. (Color online) Static droplet test: (a) density profile across the interface with different values of M_ϕ, (b) pressure distribution for $M_\phi = 0.01$, (c) spurious currents in the upper plane (MRT) and lower plane (SRT), and (d) maximum kinetic energy versus time.

the CH equation and the incompressible NS equations can be exactly recovered from the model. To test the present model, we performed a large number of numerical simulations and conducted a comprehensive comparison among different LB models. The results show that the present model is more accurate and more stable in capturing the interface. In addition, it was also found that the spurious velocity can be effectively reduced by using the present model.

As an important application, the present model was also used to study the immiscible RTI problem, in which the effect of Re is investigated in detail. It was found that the instability undergoes different growth stages at low and high values of Re. At high Re, a sequence of growth stages are obtained, including linear growth, terminal velocity, reacceleration, and chaotic development. At early stages, both the linear growth rate and the terminal Froude number quantitatively agree well with the theoretical predictions. The late chaotic stage is also observed by the present model. At this stage, the mean acceleration is found to be a constant, which indicates a quadratic growth. In contrast, at low Re, some late growth stages, such as chaotic development, could no longer be reached. Finally, we also carried out the simulation of RTI to give a comparison with the experiment and good agreement was achieved.

In conclusion, the present model can improve the performance in interface capturing and also has been proven to be promising in the study of low-viscosity or high-Reynolds-number two-phase flows; therefore, we expect that the present work can play an important role in studying complex interfacial flows.

ACKNOWLEDGMENTS

H.L. is grateful to Dr. Q. Lou for useful discussions. This work was financially supported by the National Natural Science Foundation of China (Grant No. 11272132), the National Funds for Distinguished Young Scientists of China (Grant No. 51125024), and the Fundamental Research Funds for the Central Universities (Grant No. 2014TS065).

APPENDIX A: CHAPMAN-ENSKOG ANALYSIS OF THE MRT LB MODEL FOR THE CAHN-HILLIARD EQUATION

To derive the interface governing equation (7), we first expand the order distribution function, with derivatives of time

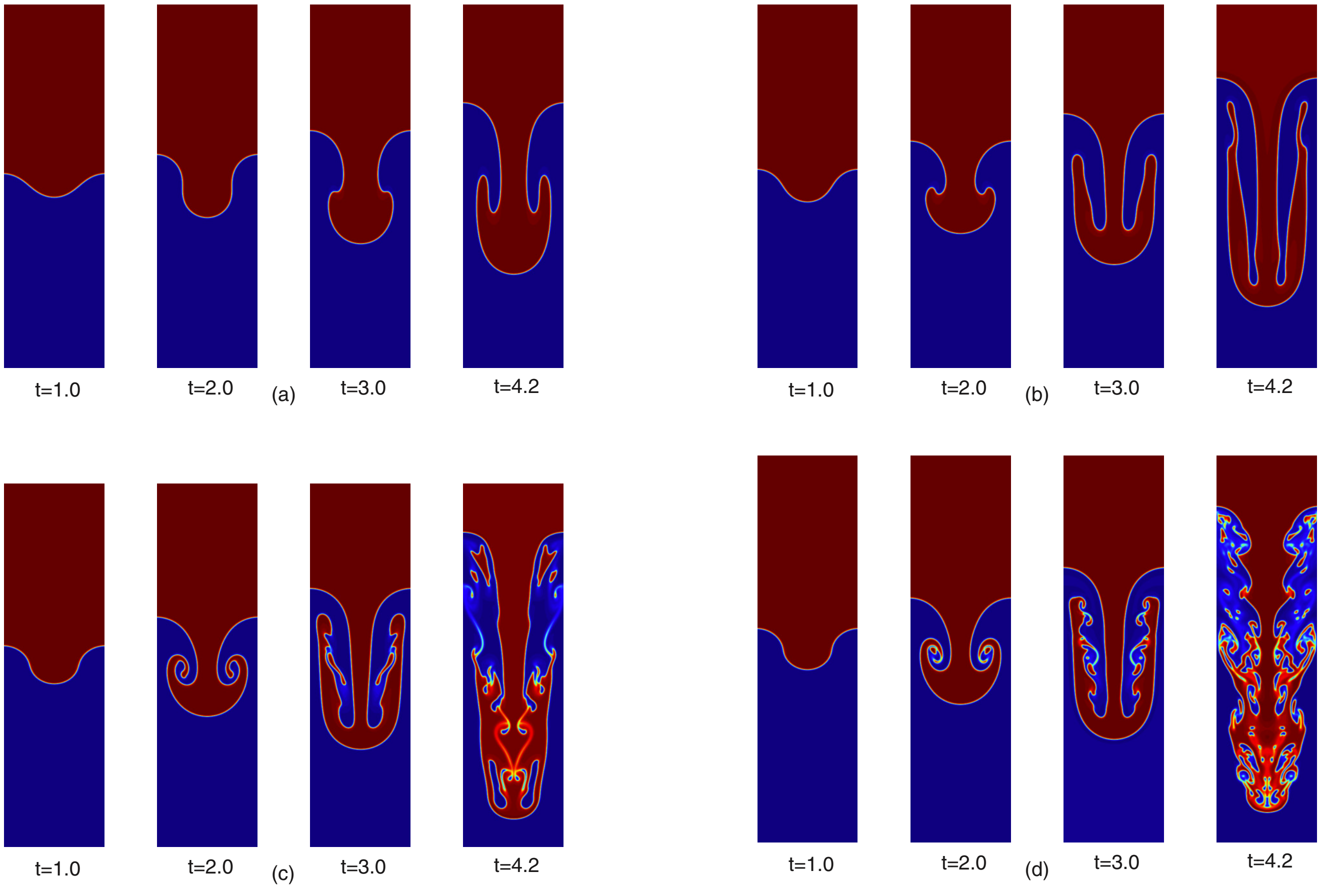

FIG. 11. (Color online) Evolution of the density contours in immiscible RTI at various values of Re: (a) Re = 30, (b) Re = 150, (c) Re = 3000, and (d) Re = 30 000. The time is normalized by the characteristic time $\sqrt{\lambda/Ag}$.

and space in consecutive scales of ϵ:

$$h_i = h_i^{(0)} + \epsilon h_i^{(1)} + \epsilon^2 h_i^{(2)} + \cdots, \tag{A1a}$$

$$\partial_t = \epsilon\partial_{t_1} + \epsilon^2\partial_{t_2}, \quad \nabla = \epsilon\nabla_1, \tag{A1b}$$

where ϵ is a small expansion parameter. By applying the Taylor expansion to Eq. (9), then it can be written as

$$D_i h_i + \frac{\delta_t}{2}D_i^2 h_i + \cdots = -\frac{1}{\delta t}(\mathbf{M}^{-1}\mathbf{S}^h\mathbf{M})_{ij}\left(h_j - h_j^{eq}\right) + R_i, \tag{A2}$$

where $D_i = \partial_t + c_i \cdot \nabla$. Substituting Eqs. (A1a)–(A1b) into Eq. (A2) and treating the terms in the zeroth, first, and second order of ϵ separately gives

$$h_i^{(0)} = h_i^{(eq)}, \tag{A3a}$$

$$D_{1i}h_i^{(0)} = -\frac{1}{\delta_t}(\mathbf{M}^{-1}\mathbf{S}^h\mathbf{M})_{ij}h_j^{(1)} + \left[\mathbf{M}^{-1}\left(\mathbf{I} - \frac{\mathbf{S}^h}{2}\right)\mathbf{M}\right]_{ij}\bar{R}_j^{(1)}, \tag{A3b}$$

$$\partial_{t_2}h_i^{(0)} + D_{1i}h_i^{(1)} + \frac{\delta_t}{2}D_{1i}^2 h_i^{(0)} = -\frac{1}{\delta_t}(\mathbf{M}^{-1}\mathbf{S}^h\mathbf{M})_{ij}h_j^{(2)} + \left[\mathbf{M}^{-1}\left(\mathbf{I} - \frac{\mathbf{S}^h}{2}\right)\mathbf{M}\right]_{ij}\bar{R}_j^{(2)} \tag{A3c}$$

for ϵ^0, ϵ^1, and ϵ^2, respectively, in which $D_{1i} = \partial_{t_1} + \mathbf{c}_i \cdot \nabla_1$, $\bar{R}_i^{(1)} = \frac{\omega_i \mathbf{c}_i \cdot \partial_{t_1}\phi\mathbf{u}}{c_s^2}$, and $\bar{R}_i^{(2)} = \frac{\omega_i \mathbf{c}_i \cdot \partial_{t_2}\phi\mathbf{u}}{c_s^2}$. Applying Eq. (A3b) to the left-hand side of Eq. (A3c) and multiplying the matrix $\mathbf{M}$ on both sides of Eqs. (A3a)–(A3c), we can obtain the following equations in the moment space:

$$\mathbf{m}_h^{(0)} = \mathbf{m}_h^{(eq)}, \tag{A4a}$$

$$\hat{\mathbf{D}}_1\mathbf{m}_h^{(0)} = -\mathbf{S}^{h'}\mathbf{m}_h^{(1)} + \left(\mathbf{I} - \frac{\mathbf{S}^h}{2}\right)\mathbf{M}\bar{\mathbf{R}}^{(1)}, \tag{A4b}$$

$$\partial_{t_2}\mathbf{m}_h^{(0)} + \hat{\mathbf{D}}_1\left(\mathbf{I} - \frac{\mathbf{S}^h}{2}\right)\mathbf{m}_h^{(1)} + \frac{\delta_t}{2}\hat{\mathbf{D}}_1\left(\mathbf{I} - \frac{\mathbf{S}^h}{2}\right)\mathbf{M}\bar{\mathbf{R}}^{(\mathbf{1})} = -\mathbf{S}^{h'}\mathbf{m}_h^{(2)} + \left(\mathbf{I} - \frac{\mathbf{S}^h}{2}\right)\mathbf{M}\bar{\mathbf{R}}^{(2)} \tag{A4c}$$

for ϵ^0, ϵ^1, and ϵ^2, respectively, where $\mathbf{S}^{h'} = \mathbf{S}^h/\delta_t$, $\hat{\mathbf{D}}_1 = \mathbf{M}\mathbf{D}_1\mathbf{M}^{-1}$, $\mathbf{D}_1 = \partial_{t_1}\mathbf{I} + \nabla_1 \cdot \mathrm{diag}(\mathbf{c}_0, \mathbf{c}_1, \ldots, \mathbf{c}_8)$, and $\mathbf{m}_h^{(1)} = (m_{h0}^{(1)}, m_{h1}^{(1)}, m_{h2}^{(1)}, m_{h3}^{(1)}, m_{h4}^{(1)}, m_{h5}^{(1)}, m_{h6}^{(1)}, m_{h7}^{(1)}, m_{h8}^{(1)})^{\mathrm{T}}$. According to Eq. (A4a), we can get

$$\mathbf{m}_h^{(0)} = \mathbf{M}\mathbf{h}^{(eq)} = \left(\phi, -4\phi + 2\eta\mu, 4\phi - 3\eta\mu, \frac{\phi u_x}{c}, \frac{-\phi u_x}{c}, \frac{\phi u_y}{c}, \frac{-\phi u_y}{c}, 0, 0\right)^{\mathrm{T}}. \tag{A5}$$

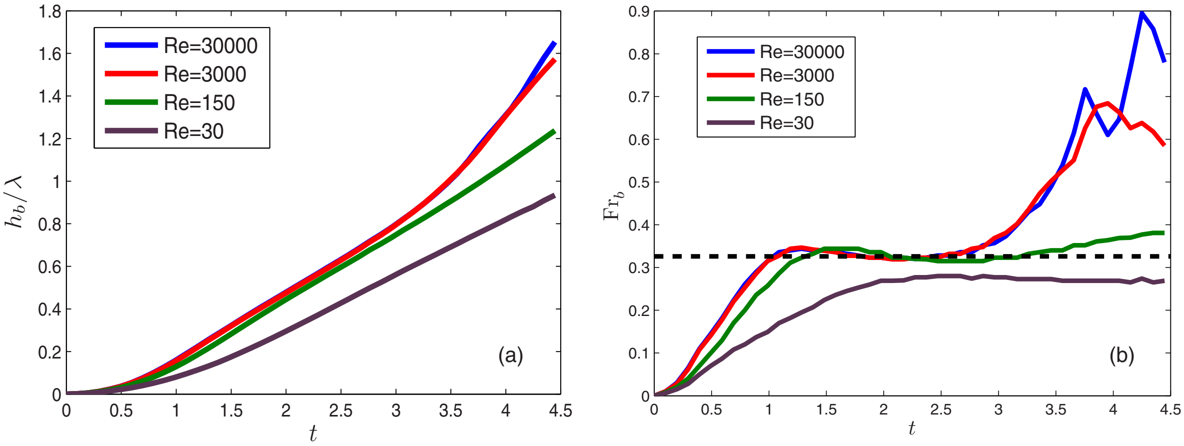

FIG. 12. (Color online) Effect of Reynolds number on (a) normalized bubble amplitude and (b) normalized bubble velocity. The time is normalized by the characteristic time $\sqrt{\lambda/Ag}$. The dashed line represents the analytical solution of the classic potential flow model [55].

Substituting Eq. (A5) into Eq. (A4b), one can obtain the following three equations associated with ϕ and $\phi\mathbf{u}$ at the ϵ scale:

$$\partial_{t_1}\phi + \partial_{x_1}\phi u_x + \partial_{y_1}\phi u_y = 0, \tag{A6a}$$

$$\partial_{t_1}\phi u_x + \partial_{x_1} c_s^2 \eta\mu = -s_3^{h'} m_{h3}^{(1)} + \left(1-\frac{s_3^h}{2}\right)\frac{\partial_{t_1}\phi u_x}{c} \tag{A6b}$$

$$\partial_{t_1}\phi u_y + \partial_{y_1} c_s^2 \eta\mu = -s_5^{h'} m_{h5}^{(1)} + \left(1-\frac{s_5^h}{2}\right)\frac{\partial_{t_1}\phi u_y}{c}. \tag{A6c}$$

Similarly, from Eq. (A4c), the equation of the conserved moment ϕ at the ϵ^2 scale can be written as

$$\partial_{t_2}\phi + \partial_{x_1}\left(1-\frac{s_3^h}{2}\right)cm_{h3}^{(1)} + \partial_{y_1}\left(1-\frac{s_5^h}{2}\right)cm_{h5}^{(1)} + \frac{\delta_t}{2}\partial_{x_1}\left(1-\frac{s_3^h}{2}\right)\partial_{t_1}\phi u_x + \frac{\delta_t}{2}\partial_{y_1}\left(1-\frac{s_5^h}{2}\right)\partial_{t_1}\phi u_y = 0. \tag{A7}$$

Note that $m_{h3}^{(1)}$ and $m_{h5}^{(1)}$ are unknown and will be determined below. With the aid of Eqs. (A6b) and (A6c), we can get

$$s_3^{h'} m_{h3}^{(1)} = -\partial_{t_1}\phi u_x - \partial_{x_1} c_s^2\eta\mu + \left(1-\frac{s_3^h}{2}\right)\frac{\partial_{t_1}\phi u_x}{c}, \tag{A8a}$$

$$s_5^{h'} m_{h5}^{(1)} = -\partial_{t_1}\phi u_y - \partial_{y_1} c_s^2\eta\mu + \left(1-\frac{s_5^h}{2}\right)\frac{\partial_{t_1}\phi u_y}{c}. \tag{A8b}$$

Substituting Eqs. (A8a) and (A8b) into Eq. (A7), the second-order equation in ϵ is rewritten as

$$\partial_{t_2}\phi = \partial_{x_1}\left[\eta c_s^2\delta_t\left(\frac{1}{s_3^h}-\frac{1}{2}\right)\partial_{x_1}\mu\right] + \partial_{y_1}\left[\eta c_s^2\delta_t\left(\frac{1}{s_5^h}-\frac{1}{2}\right)\partial_{y_1}\mu\right]. \tag{A9}$$

For the isotropic diffusion considered here, the relation $s_3^h = s_5^h$ should be satisfied. Combining Eq. (A6a) at t_1 time scale and Eq. (A9) at t_2 time scale, we can obtain the recovered CH equation

$$\frac{\partial\phi}{\partial t} + \nabla\cdot\phi\mathbf{u} = \nabla\cdot M_\phi(\nabla\mu), \tag{A10}$$

where $M_\phi = \eta c_s^2\delta_t(\frac{1}{s_3^h}-\frac{1}{2})$ is the mobility.

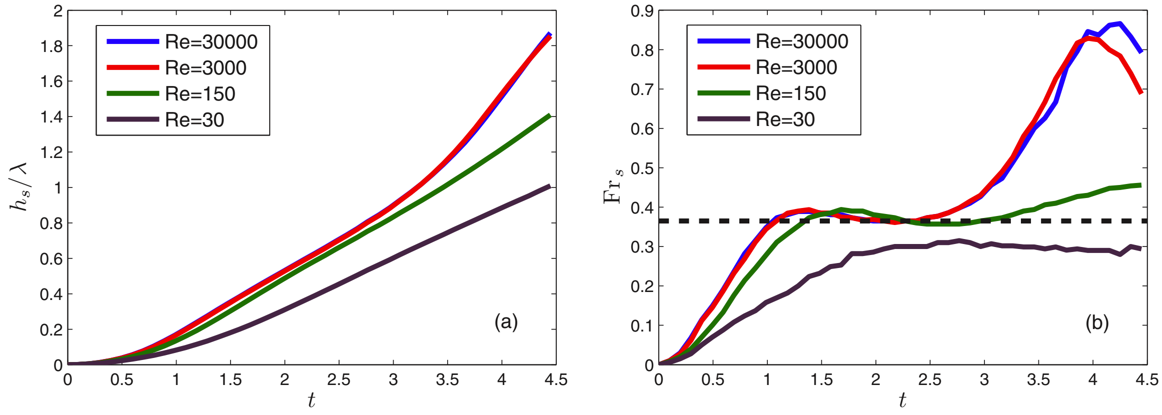

FIG. 13. (Color online) Effect of Reynolds number on (a) normalized spike amplitude and (b) normalized spike velocity. The time is normalized by the characteristic time $\sqrt{\lambda/Ag}$. The dashed line represents the analytical solution of the classic potential flow model [55].

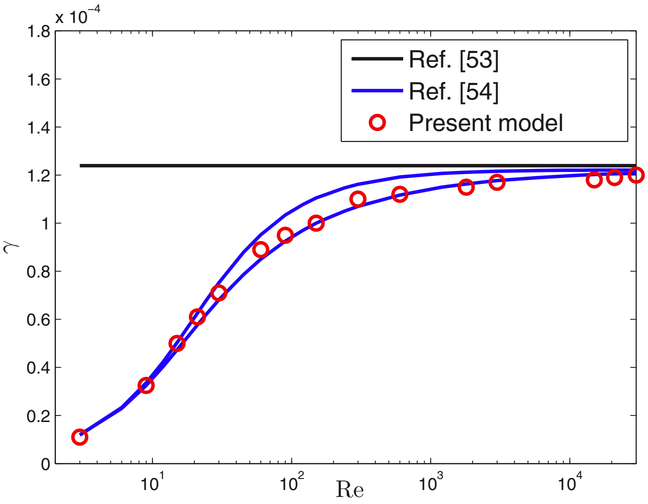

FIG. 14. (Color online) Dependence of the linear growth rate γ on Reynolds numbers.

APPENDIX B: CHAPMAN-ENSKOG ANALYSIS OF THE MRT LB MODEL FOR THE INCOMPRESSIBLE HYDRODYNAMIC EQUATIONS

In this section, the proposed model for hydrodynamic equations is analyzed by applying the Chapman-Enskog expansion

$$\bar{g}_i = \bar{g}_i^{(0)} + \epsilon \bar{g}_i^{(1)} + \epsilon^2 \bar{g}_i^{(2)} + \cdots, \tag{B1a}$$

$$\partial_t = \epsilon \partial_{t_1} + \epsilon^2 \partial_{t_2}, \quad \nabla = \epsilon \nabla_1, \quad F_i = \epsilon {F_i}^{(1)}. \tag{B1b}$$

Using the Taylor expansion in Eq. (29), one can obtain

$$D_i \bar{g}_i + \frac{\delta_t}{2} D_i^2 \bar{g}_i + \cdots = -\frac{1}{\delta_t} (\mathbf{M}^{-1}\mathbf{S}^g\mathbf{M})_{ij} \left(\bar{g}_j - g_j^{eq}\right) + \left[\mathbf{M}^{-1}\left(\mathrm{I} - \frac{\mathbf{S}^g}{2}\right)\mathbf{M}\right]_{ij} F_j. \tag{B2}$$

Based on Eqs. (B1a) and (B1b), we can rewrite Eq. (B2) in consecutive orders of the parameter ϵ as

$$\bar{g}_i^{(0)} = g_i^{(eq)}, \tag{B3a}$$

$$D_{1i} \bar{g}_i^{(0)} = -\frac{1}{\delta_t} (\mathbf{M}^{-1}\mathbf{S}^g\mathbf{M})_{ij} \bar{g}_j^{(1)} + \left[\mathbf{M}^{-1}\left(\mathbf{I} - \frac{\mathbf{S}^g}{2}\right)\mathbf{M}\right]_{ij} {F_j}^{(1)}, \tag{B3b}$$

$$\partial_{t_2} \bar{g}_i^{(0)} + D_{1i} \bar{g}_i^{(1)} + \frac{\delta_t}{2} D_{1i}^2 \bar{g}_i^{(0)} = -\frac{1}{\delta_t} (\mathbf{M}^{-1}\mathbf{S}^g\mathbf{M})_{ij} \bar{g}_j^{(2)} \tag{B3c}$$

for ϵ^0, ϵ^1, and ϵ^2, respectively. Multiplying matrix $\mathbf{M}$ on the both sides of Eqs. (B3a)–(B3c) yields the corresponding moment equations

$$\mathbf{m}_g^{(0)} = \mathbf{m}_g^{(eq)}, \tag{B4a}$$

$$\hat{\mathbf{D}}_1 \mathbf{m}_g^{(0)} = -\mathbf{S}^{g'} \bar{\mathbf{m}}_g^{(1)} + \left(\mathbf{I} - \frac{\mathbf{S}^g}{2}\right) \mathbf{M} \bar{\mathbf{F}}^{(1)}, \tag{B4b}$$

$$\partial_{t_2} \mathbf{m}_g^{(0)} + \hat{\mathbf{D}}_1 \left(\mathbf{I} - \frac{\mathbf{S}^g}{2}\right) \bar{\mathbf{m}}_g^{(1)} + \frac{\delta_t}{2} \hat{\mathbf{D}}_1 \left(\mathbf{I} - \frac{\mathbf{S}^g}{2}\right) \mathbf{M} \bar{\mathbf{F}}^{(1)} = -\mathbf{S}^{g'} \bar{\mathbf{m}}_g^{(2)} \tag{B4c}$$

for ϵ^0, ϵ^1, and ϵ^2, respectively, where $\mathbf{S}^{g'} = \mathbf{S}^g/\delta_t$, $\bar{\mathbf{m}}_g$, $\mathbf{m}_g^{(0)}$, $\bar{\mathbf{m}}_g^{(1)}$, and $\bar{\mathbf{m}}_g^{(k)}$ ($k \geqslant 2$) are given by

$$\bar{\mathbf{m}}_g = \mathbf{M}\bar{\mathbf{g}} = \left(-\frac{\delta_t}{2} \mathbf{u} \cdot \nabla \rho, \bar{m}_{g1}, \bar{m}_{g2}, \frac{\rho u_x}{c} - \frac{\delta_t F_x}{2c}, \bar{m}_{g4}, \frac{\rho u_y}{c} - \frac{\delta_t F_y}{2c}, \bar{m}_{g6}, \bar{m}_{g7}, \bar{m}_{g8}\right)^{\mathrm{T}}, \tag{B5a}$$

$$\mathbf{m}_g^{(0)} = \mathbf{M}\mathbf{g}^{(eq)} = \left(0, \frac{2p + \rho u_x^2 + \rho u_y^2}{c_s^2}, \frac{-3p - \rho u_x^2 - \rho u_y^2}{c_s^2}, \frac{\rho u_x}{c}, -\frac{\rho u_x}{c}, \frac{\rho u_y}{c}, -\frac{\rho u_y}{c}, \frac{\rho u_x^2 - \rho u_y^2}{c^2}, \frac{\rho u_x u_y}{c^2}\right)^{\mathrm{T}}, \tag{B5b}$$

$$\bar{\mathbf{m}}_g^{(1)} = \left(-\frac{\delta_t}{2} \mathbf{u} \cdot \nabla_1 \rho, \bar{m}_{g1}^{(1)}, \bar{m}_{g2}^{(1)}, -\frac{\delta_t {F_x}^{(1)}}{2c}, \bar{m}_{g4}^{(1)}, -\frac{\delta_t {F_y}^{(1)}}{2c}, \bar{m}_{g6}^{(1)}, \bar{m}_{g7}^{(1)}, \bar{m}_{g8}^{(1)}\right), \tag{B5c}$$

$$\bar{\mathbf{m}}_g^{(k)} = \left(0, \bar{m}_{g1}^{(k)}, \bar{m}_{g2}^{(k)}, 0, \bar{m}_{g4}^{(k)}, 0, \bar{m}_{g6}^{(k)}, \bar{m}_{g7}^{(k)}, \bar{m}_{g8}^{(k)}\right) \quad (k \geqslant 2), \tag{B5d}$$

where $\mathbf{g}^{(eq)} = (g_0^{(eq)}, g_1^{(eq)}, g_2^{(eq)}, g_3^{(eq)}, g_4^{(eq)}, g_5^{(eq)}, g_6^{(eq)}, g_7^{(eq)}, g_8^{(eq)})^{\mathrm{T}}$, $F_x = F_{sx} + F_{ax} + G_x$, $F_y = F_{sy} + F_{ay} + G_y$, ${F_x}^{(1)} = {F_{sx}}^{(1)} + {F_{ax}}^{(1)} + {G_x}^{(1)}$, and ${F_y}^{(1)} = {F_{sy}}^{(1)} + {F_{ay}}^{(1)} + {G_y}^{(1)}$. Substituting Eqs. (B5b) and (B5c) into Eq. (B4b), one can directly derive several first-order equations in ϵ. For simplicity, however, only those related to the hydrodynamic equations are presented:

$$\partial_{x_1} u_x + \partial_{y_1} u_y = 0, \tag{B6a}$$

$$\partial_{t_1} \rho u_x + \partial_{x_1} \left(p + \rho u_x^2\right) + \partial_{y_1} \rho u_x u_y = F_x^{(1)}, \tag{B6b}$$

$$\partial_{t_1} \rho u_y + \partial_{x_1} \rho u_x u_y + \partial_{y_1} \left(p + \rho u_y^2\right) = F_y^{(1)}, \tag{B6c}$$

$$\partial_{t_1} \frac{2p + \rho u_x^2 + \rho u_y^2}{c_s^2} = -s_1^{g'} \bar{m}_{g_1}^{(1)} + F_{g_1}, \tag{B6d}$$

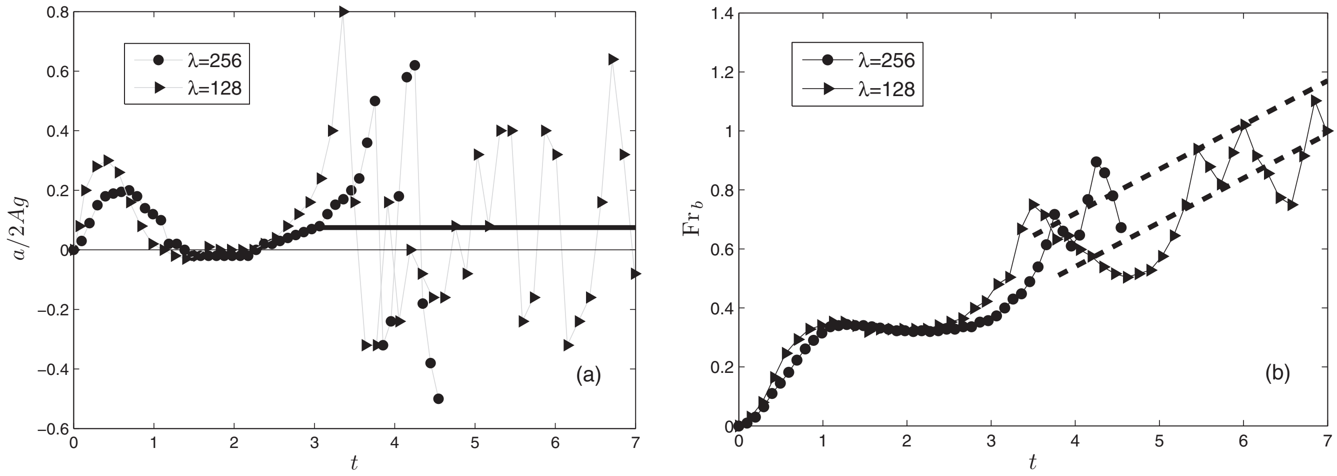

FIG. 15. (a) Normalized bubble acceleration and (b) bubble Froude number versus dimensionless time at high Re. The solid line represents the value of 0.07. The dashed lines have a slope of 0.15.

$$\partial_{t_1}\frac{\rho u_x^2-\rho u_y^2}{c^2}+\partial_{x_1}\frac{2\rho u_x}{3}-\partial_{y_1}\frac{2\rho u_y}{3}=-s_7^{g'}\bar{m}_{g_7}^{(1)}+F_{g_7}, \tag{B6e}$$

$$\partial_{t_1}\frac{\rho u_x u_y}{c^2}+\partial_{x_1}\frac{\rho u_y}{3}+\partial_{y_1}\frac{\rho u_x}{3}=-s_8^{g'}\bar{m}_{g_8}^{(1)}+F_{g_8}, \tag{B6f}$$

where

$$F_{g_1}=\left(1-\frac{s_1^g}{2}\right)\left(\frac{6}{c^2}\mathbf{u}\cdot\mathbf{F}^{(1)}-\frac{9}{c^4}(\mathbf{u}\cdot\mathbf{u})\big[\mathbf{u}\cdot\big(\mathbf{F}^{(1)}+\nabla_1\rho c_s^2\big)\big]\right), \tag{B7a}$$

$$F_{g_7}=\left(1-\frac{s_7^g}{2}\right)\left(\frac{2}{c^2}\big[u_x\big(F_x^{(1)}+\nabla_{1x}\rho c_s^2\big)-u_y\big(F_y^{(1)}+\nabla_{1y}\rho c_s^2\big)\big]-\frac{3}{c^4}\big(u_x^2-u_y^2\big)\big[\mathbf{u}\cdot\big(\mathbf{F}^{(1)}+\nabla_1\rho c_s^2\big)\big]\right), \tag{B7b}$$

$$F_{g_8}=\left(1-\frac{s_8^g}{2}\right)\left(\frac{1}{c^2}\big[u_x\big(F_y^{(1)}+\nabla_{1y}\rho c_s^2\big)+u_y\big(F_x^{(1)}+\nabla_{1x}\rho c_s^2\big)\big]-\frac{3}{c^4}u_x u_y\big[\mathbf{u}\cdot\big(\mathbf{F}^{(1)}+\nabla_1\rho c_s^2\big)\big]\right). \tag{B7c}$$

Note that $\mathbf{F}^{(1)}$ in Eqs. (B7a)–(B7c) is defined as $\mathbf{F}^{(1)}=(F_x^{(1)},F_y^{(1)})$. In a similar fashion, from Eq. (B4c), the second-order equations in ϵ can also be obtained:

$$\partial_{t_2}\rho u_x+\frac{c^2}{6}\partial_{x_1}\left(1-\frac{s_1^g}{2}\right)\bar{m}_{g1}^{(1)}+\frac{c^2}{2}\partial_{x_1}\left(1-\frac{s_7^g}{2}\right)\bar{m}_{g7}^{(1)}+c^2\partial_{y_1}\left(1-\frac{s_8^g}{2}\right)\bar{m}_{g8}^{(1)}+F_{gx178}=0, \tag{B8a}$$

$$\partial_{t_2}\rho u_y+\frac{c^2}{6}\partial_{y_1}\left(1-\frac{s_1^g}{2}\right)\bar{m}_{g1}^{(1)}-\frac{c^2}{2}\partial_{y_1}\left(1-\frac{s_7^g}{2}\right)\bar{m}_{g7}^{(1)}+c^2\partial_{x_1}\left(1-\frac{s_8^g}{2}\right)\bar{m}_{g8}^{(1)}+F_{gy178}=0, \tag{B8b}$$

where F_{gx178} and F_{gy178} are given by

$$\begin{aligned}F_{gx178}=&\frac{\delta_t}{2}\partial_{x_1}\left(1-\frac{s_1^g}{2}\right)\left(\mathbf{u}\cdot\mathbf{F}^{(1)}-\frac{3}{2c^2}(\mathbf{u}\cdot\mathbf{u})\big[\mathbf{u}\cdot\big(\mathbf{F}^{(1)}+\nabla_1\rho c_s^2\big)\big]\right)\\&+\frac{\delta_t}{2}\partial_{x_1}\left(1-\frac{s_7^g}{2}\right)\left(\big[u_x\big(F_x^{(1)}+\nabla_{1x}\rho c_s^2\big)-u_y\big(F_y^{(1)}+\nabla_{1y}\rho c_s^2\big)\big]-\frac{3}{2c^2}\big(u_x^2-u_y^2\big)\big[\mathbf{u}\cdot\big(\mathbf{F}^{(1)}+\nabla_1\rho c_s^2\big)\big]\right)\\&+\frac{\delta_t}{2}\partial_{y_1}\left(1-\frac{s_8^g}{2}\right)\left(\big[u_x\big(F_y^{(1)}+\nabla_{1y}\rho c_s^2\big)+u_y\big(F_x^{(1)}+\nabla_{1x}\rho c_s^2\big)\big]-\frac{3}{c^2}u_x u_y\big[\mathbf{u}\cdot\big(\mathbf{F}^{(1)}+\nabla_1\rho c_s^2\big)\big]\right)\end{aligned} \tag{B9}$$

and

$$\begin{aligned}F_{gy178}=&\frac{\delta_t}{2}\partial_{y_1}\left(1-\frac{s_1^g}{2}\right)\left(\mathbf{u}\cdot\mathbf{F}^{(1)}-\frac{3}{2c^2}(\mathbf{u}\cdot\mathbf{u})\big[\mathbf{u}\cdot\big(\mathbf{F}^{(1)}+\nabla_1\rho c_s^2\big)\big]\right)\\&-\frac{\delta_t}{2}\partial_{y_1}\left(1-\frac{s_7^g}{2}\right)\left(\big[u_x\big(F_x^{(1)}+\nabla_{1x}\rho c_s^2\big)-u_y\big(F_y^{(1)}+\nabla_{1y}\rho c_s^2\big)\big]-\frac{3}{2c^2}\big(u_x^2-u_y^2\big)\big[\mathbf{u}\cdot\big(\mathbf{F}^{(1)}+\nabla_1\rho c_s^2\big)\big]\right)\\&+\frac{\delta_t}{2}\partial_{x_1}\left(1-\frac{s_8^g}{2}\right)\left(\big[u_x\big(F_y^{(1)}+\nabla_{1y}\rho c_s^2\big)+u_y\big(F_x^{(1)}+\nabla_{1x}\rho c_s^2\big)\big]-\frac{3}{c^2}u_x u_y\big[\mathbf{u}\cdot\big(\mathbf{F}^{(1)}+\nabla_1\rho c_s^2\big)\big]\right),\end{aligned} \tag{B10}$$

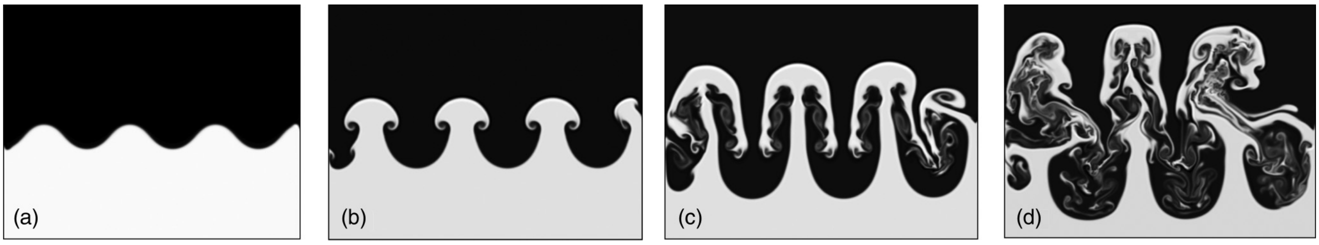

FIG. 16. Evolution of the density contours in immiscible RTI at $A = 0.336$ and $\mathrm{Re} = 10\,000$ for (a) $t = 0.067$ s, (b) $t = 0.133$ s, (c) $t = 0.231$ s, and (d) $t = 0.297$ s.

respectively. Note that $\bar{m}_{g1}^{(1)}$, $\bar{m}_{g7}^{(1)}$, and $\bar{m}_{g8}^{(1)}$ in Eqs. (B8a) and (B8b) are unknown and will be determined in the following. Using Eqs. (B6d)–(B6f) and neglecting the terms (related to u^3 and $u\nabla p$) of $O(Ma^3)$, we can get

$$-s_1^{g'}\bar{m}_{g_1}^{(1)} = \frac{3s_1^g}{c^2}\mathbf{u}\cdot\mathbf{F}^{(1)} - \partial_{t_1}\frac{2p}{c_s^2} - \frac{(\mathbf{u}\cdot\mathbf{u})\partial_{t_1}\rho}{c_s^2}, \tag{B11a}$$

$$-s_7^{g'}\bar{m}_{g_7}^{(1)} = \frac{2}{3}\rho(\partial_{x_1}u_x - \partial_{y_1}u_y) + \frac{s_7^g}{c^2}\left[u_x\left(F_x^{(1)} + \nabla_{1x}\rho c_s^2\right) - u_y\left(F_y^{(1)} + \nabla_{1y}\rho c_s^2\right)\right] - \frac{u_x^2 - u_y^2}{c^2}\partial_{t_1}\rho, \tag{B11b}$$

$$-s_8^{g'}\bar{m}_{g_8}^{(1)} = \frac{\rho}{3}(\partial_{x_1}u_y + \partial_{y_1}u_x) + \frac{s_8^g}{2c^2}\left[u_x\left(F_y^{(1)} + \nabla_{1y}\rho c_s^2\right) + u_y\left(F_x^{(1)} + \nabla_{1x}\rho c_s^2\right)\right] - \frac{u_xu_y}{c^2}\partial_{t_1}\rho. \tag{B11c}$$

The substitution of the above results into Eqs. (B8a) and (B8b) gives

$$\partial_{t_2}\rho u_x - \partial_{x_1}\nu\rho(2\partial_{x_1}u_x) - \partial_{y_1}\nu\rho(\partial_{y_1}u_x + \partial_{x_1}u_y) + T_1 = 0, \tag{B12a}$$

$$\partial_{t_2}\rho u_y - \partial_{x_1}\nu\rho(\partial_{x_1}u_y + \partial_{y_1}u_x) - \partial_{y_1}\nu\rho(2\partial_{y_1}u_y) + T_2 = 0, \tag{B12b}$$

where

$$\nu = c_s^2\delta_t\left(\frac{1}{s_7^g} - \frac{1}{2}\right) = c_s^2\delta_t\left(\frac{1}{s_8^g} - \frac{1}{2}\right), \tag{B13}$$

$$T_1 = \partial_{x_1}\left(\frac{1}{s_1^g} - \frac{1}{2}\right)\delta_t\left(\partial_{t_1}p + \frac{\mathbf{u}\cdot\mathbf{u}}{2}\partial_{t_1}\rho\right) + \partial_{x_1}\left(\frac{1}{s_7^g} - \frac{1}{2}\right)\delta_t\frac{u_x^2 - u_y^2}{2}\partial_{t_1}\rho + \partial_{y_1}\left(\frac{1}{s_8^g} - \frac{1}{2}\right)\delta_t u_xu_y\partial_{t_1}\rho, \tag{B14}$$

and

$$T_2 = \partial_{y_1}\left(\frac{1}{s_1^g} - \frac{1}{2}\right)\delta_t\left(\partial_{t_1}p + \frac{\mathbf{u}\cdot\mathbf{u}}{2}\partial_{t_1}\rho\right) + \partial_{y_1}\left(\frac{1}{s_7^g} - \frac{1}{2}\right)\delta_t\frac{u_y^2 - u_x^2}{2}\partial_{t_1}\rho + \partial_{x_1}\left(\frac{1}{s_8^g} - \frac{1}{2}\right)\delta_t u_xu_y\partial_{t_1}\rho. \tag{B15}$$

Under the incompressible condition [$\partial_{t_1}p = O(Ma^2)$ and $\mathbf{u}^2 = O(Ma^2)$], we can get $T_1 = O(\delta_t Ma^2)$ and $T_2 = O(\delta_t Ma^2)$. Therefore, Eqs. (B12a) and (B12b) can be simplified as

$$\partial_{t_2}\rho u_x - \partial_{x_1}\nu\rho(\partial_{x_1}u_x - \partial_{y_1}u_y) - \partial_{y_1}\nu\rho(\partial_{y_1}u_x + \partial_{x_1}u_y) = 0, \tag{B16a}$$

$$\partial_{t_2}\rho u_y - \partial_{x_1}\nu\rho(\partial_{x_1}u_y + \partial_{y_1}u_x) - \partial_{y_1}\nu\rho(\partial_{y_1}u_y - \partial_{x_1}u_x) = 0. \tag{B16b}$$

Combining Eqs. (B6a)–(B6c) and Eqs. (B16a) and (B16b) at different time scales, we can obtain the hydrodynamic equations

$$\nabla\cdot\mathbf{u} = 0, \tag{B17a}$$

$$\frac{\partial\rho\mathbf{u}}{\partial t} + \nabla\cdot\rho\mathbf{u}\mathbf{u} = -\nabla p + \nabla\cdot[\nu\rho(\nabla\mathbf{u} + \nabla\mathbf{u}^T)] + \mathbf{F}_s + \mathbf{F}_a + \mathbf{G}. \tag{B17b}$$

Furthermore, using the relationship

$$\partial_t\rho + \nabla\cdot\rho\mathbf{u} = \frac{\partial\rho}{\partial\phi}(\partial_t\phi + \nabla\cdot\phi\mathbf{u}) = \frac{\partial\rho}{\partial\phi}\nabla\cdot M_\phi(\nabla\mu), \tag{B18}$$

we have

$$\frac{\partial\rho\mathbf{u}}{\partial t} + \nabla\cdot\rho\mathbf{u}\mathbf{u} = \rho\left(\frac{\partial\mathbf{u}}{\partial t} + \mathbf{u}\cdot\nabla\mathbf{u}\right) + \mathbf{F}_a \tag{B19}$$

Based on the above result, Eqs. (B17a) and (B17b) can reduce to the incompressible Navier-Stokes equations (8). That is to say, the LB equation, i.e., Eq. (29), can exactly recover the hydrodynamic equations for incompressible multiphase fluids.

Now we discuss how to calculate the pressure p from the distribution function $\bar{g}_i$. Starting from the expression of $g_0^{(eq)}$, we have

$$g_0^{(eq)}(\mathbf{x},t) = \frac{\omega_0 - 1}{c_s^2}p(\mathbf{x},t) + \rho s_0[\mathbf{u}(\mathbf{x},t)] \tag{B20}$$

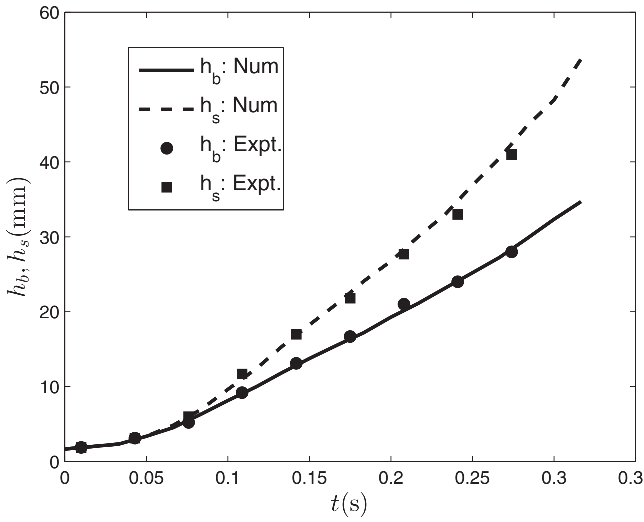

FIG. 17. Comparison between the present results with experiments [52]. Here h_b and h_s represent the bubble and spike amplitudes.

and also

$$\bar{g}_0(\mathbf{x},t) - \left[\bar{g}_0(\mathbf{x},t) - g_0^{(eq)}(\mathbf{x},t)\right] = \frac{\omega_0 - 1}{c_s^2} p(\mathbf{x},t) + \rho s_0[\mathbf{u}(\mathbf{x},t)]. \tag{B21}$$

Next we evaluate $[\bar{g}_0(\mathbf{x},t) - g_0^{(eq)}(\mathbf{x},t)]$. From Eq. (B3b) we can derive

$$(\mathbf{M}^{-1}\mathbf{S}^g\mathbf{M})_{ij}\left[\bar{g}_j(\mathbf{x},t) - g_j^{eq}(\mathbf{x},t)\right] = -\delta_t D_i \bar{g}_i(\mathbf{x},t) + \delta_t\left[\mathbf{M}^{-1}\left(\mathbf{I} - \frac{\mathbf{S}^g}{2}\right)\mathbf{M}\right]_{ij} F_j(\mathbf{x},t) + O\left(\delta_t^2\right). \tag{B22}$$

Multiplying the matrix $\mathbf{M}^{-1}\mathbf{S}^{g\,-1}\mathbf{M}$ on both sides of Eq. (B22), one can obtain

$$\bar{g}_i(\mathbf{x},t) - g_i^{eq}(\mathbf{x},t) = -\delta_t(\mathbf{M}^{-1}\mathbf{S}^{g\,-1}\mathbf{M})_{ij} D_j \bar{g}_j(\mathbf{x},t) + \delta_t\left[\mathbf{M}^{-1}\left(\mathbf{S}^{g\,-1} - \frac{\mathbf{I}}{2}\right)\mathbf{M}\right]_{ij} F_j(\mathbf{x},t) + O(\delta_t^2), \tag{B23}$$

which shows that

$$\bar{g}_i(\mathbf{x},t) = g_i^{eq}(\mathbf{x},t) + O(\delta_t). \tag{B24}$$

Substituting Eq. (B24) into Eq. (B23) yields

$$\bar{g}_i(\mathbf{x},t) - g_i^{eq}(\mathbf{x},t) = -\delta_t(\mathbf{M}^{-1}\mathbf{S}^{g\,-1}\mathbf{M})_{ij} D_j g_j^{eq}(\mathbf{x},t) + \delta_t\left[\mathbf{M}^{-1}\left(\mathbf{S}^{g\,-1} - \frac{\mathbf{I}}{2}\right)\mathbf{M}\right]_{ij} F_j(\mathbf{x},t) + O\left(\delta_t^2\right). \tag{B25}$$

With some algebraic operations and taking $i = 0$, we have

$$\bar{g}_0(\mathbf{x},t) - g_0^{eq}(\mathbf{x},t) = \left(\frac{3s_1^g + 2s_2^g}{3c^2 s_1^g s_2^g}\right)\delta_t \frac{\partial p}{\partial t} + \left(\frac{s_1^g + s_2^g}{3c^2 s_1^g s_2^g}\right) \times \delta_t \frac{\partial \rho \mathbf{u}\cdot\mathbf{u}}{\partial t} + \frac{2\left(s_1^g s_2^g - s_1^g - s_2^g\right)}{3c^2 s_1^g s_2^g} \times \delta_t(u_x F_x + u_y F_y) + O\left(\delta_t{}^2\right). \tag{B26}$$

From Eqs. (B6b) and (B6c) we know that $F_{x,y} = O(Ma)$ and under the incompressible condition, Eq. (B26) can be rewritten as

$$\bar{g}_0(\mathbf{x},t) - g_0^{eq}(\mathbf{x},t) = O\left(\delta_t{}^2 + \delta_t Ma^2\right). \tag{B27}$$

Therefore, we can neglect the terms in square brackets on the left-hand side of Eq. (B21) and the pressure can be presented as

$$\frac{\omega_0 - 1}{c_s^2} p = \bar{g}_0 - \rho s_0(\mathbf{u}) + O\left(\delta_t^2 + \delta_t Ma^2\right). \tag{B28}$$

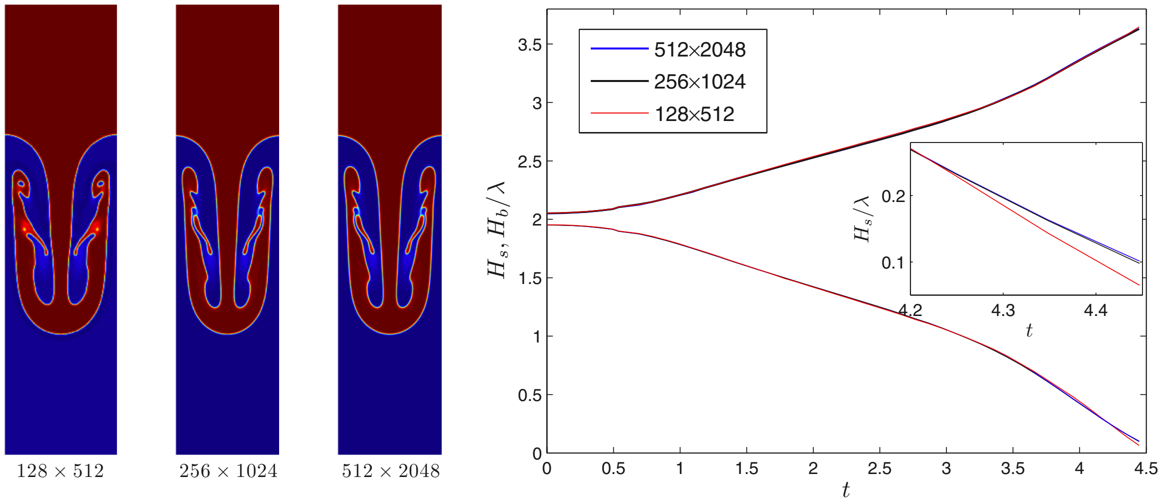

(a) (b)

FIG. 18. (Color online) Grid-independent test for Re = 3000: (a) the interface patterns at $t = 3.0$ and (b) the positions of the bubble and spike fronts versus dimensionless time.

Based on Eq. (24), we get

$$\sum_i \bar{g}_i = -\frac{\delta_t}{2}\mathbf{u}\cdot\nabla\rho. \tag{B29}$$

As a result, the pressure can be calculated as

$$p = \frac{c_s^2}{1-\omega_0}\left[\sum_{i\neq 0}\bar{g}_i + \rho s_0(\mathbf{u}) + \frac{\delta_t}{2}\mathbf{u}\cdot\nabla\rho\right], \tag{B30}$$

which has an accuracy of $O(\delta_t^2 + \delta_t Ma^2)$.

APPENDIX C: GRID-INDEPENDENCE TEST

To ensure that the numerical results are grid independent, the grid resolution test is conducted by simulating a case with Re = 3000 on three different sets of grids: 512 × 128, 1024 × 256, and 2048 × 512. The interface patterns at $t = 3.0$ and the positions of the bubble and spike fronts are presented in Figs. 18(a) and 18(b), respectively. Figure 18(a) clearly shows that the intermediate grid provides sufficient accuracy in capturing the structures of small vortices. In addition, Fig. 18(b) shows that the position of the bubble front is well captured using the coarse grid, but it needs at least the intermediate grid to obtain the accurate position of the spike front. Therefore, the intermediate grid has already given grid-independent results and will be adopted in simulations of immiscible RTI.

APPENDIX D: BOUNDS OF THE GROWTH RATE FOR VISCOUS FLUIDS

It is substantially difficult to give an analytical growth rate including the effect of viscosity [53]. However, the lower and upper bounds to the growth rate can be presented, which satisfy the following equations respectively [54]:

$$\gamma_\nu^4 + \nu k^2\gamma_\nu^3 - 2\gamma^2\gamma_\nu^2 - 2\nu k^2\gamma^2\gamma_\nu + \gamma^4 = 0, \tag{D1}$$

$$\gamma_\nu^2 + 2\nu k^2\gamma_\nu - \gamma^2 = 0, \tag{D2}$$

where γ is the growth rate for inviscid fluids given in Eq. (41). One can easily obtain the upper bound γ_u by solving Eq. (D2),

$$\gamma_u = -\nu k^2 + \sqrt{\nu^2k^4 + \gamma^2}, \tag{D3}$$

while the lower bound is a real solution of Eq. (D1) and should be smaller than γ_u.

[1] S. Unverdi and G. Tryggvason, J. Comput. Phys. **100**, 25 (1992).
[2] M. Sussman, P. Smereka, and S. Osher, J. Comput. Phys. **114**, 146 (1994).
[3] D. M. Anderson, G. B. McFadden, and A. A. Wheeler, Annu. Rev. Fluid Mech. **30**, 139 (1998).
[4] D. Jacqmin, J. Comput. Phys. **155**, 96 (1999).
[5] S. Chen and G. Doolen, Annu. Rev. Fluid Mech. **30**, 329 (1998).
[6] S. Succi, *The Lattice Boltzmann Equation for Fluid Dynamics and Beyond* (Oxford University Press, Oxford, 2001).
[7] R. R. Nourgaliev, T. N. Dinh, T. G. Theofanous, and D. Joseph, Int. J. Multiphase Flow **29**, 117 (2003).
[8] C. K. Aidun and J. R. Clausen, Annu. Rev. Fluid Mech. **42**, 439 (2010).
[9] A. K. Gunstensen, D. H. Rothman, S. Zaleski, and G. Zanetti, Phys. Rev. A **43**, 4320 (1991).
[10] D. H. Rothman and J. M. Keller, J. Stat. Phys. **52**, 1119 (1988).
[11] X. Shan and H. Chen, Phys. Rev. E **47**, 1815 (1993).
[12] X. Shan and H. Chen, Phys. Rev. E **49**, 2941 (1994).
[13] S. Hou, X. Shan, Q. Zou, G. D. Doolen, and W. E. Soll, J. Comput. Phys. **138**, 695 (1997).
[14] M. R. Swift, W. R. Osborn, and J. M. Yeomans, Phys. Rev. Lett. **75**, 830 (1995).
[15] M. R. Swift, E. Orlandini, W. R. Osborn, and J. M. Yeomans, Phys. Rev. E **54**, 5041 (1996).
[16] T. Inamuro, N. Konishi, and F. Ogino, Comput. Phys. Commun. **129**, 32 (2000).
[17] A. N. Kalarakis, V. N. Burganos, and A. C. Payatakes, Phys. Rev. E **65**, 056702 (2002).
[18] T. Inamuro, T. Ogata, S. Tajima, and N. Konishi, J. Comput. Phys. **198**, 628 (2004).
[19] L. S. Luo, Phys. Rev. Lett. **81**, 1618 (1998); Phys. Rev. E **62**, 4982 (2000).
[20] Z. L. Guo and T. S. Zhao, Phys. Rev. E **68**, R035302 (2003).
[21] X. He, X. Shan, and G. D. Doolen, Phys. Rev. E **57**, R13 (1998).
[22] X. He, S. Chen, and R. Zhang, J. Comput. Phys. **152**, 642 (1999).
[23] T. Lee and C. L. Lin, J. Comput. Phys. **206**, 16 (2005).
[24] T. Lee and L. Liu, J. Comput. Phys. **229**, 8045 (2010).
[25] A. Fakhari and T. Lee, Phys. Rev. E **87**, 023304 (2013).
[26] D. Chiappini, G. Bella, S. Succi, F. Toschi, and S. Ubertini, Commun. Comput. Phys. **7**, 423 (2010).
[27] Z. L. Guo, C. G. Zheng, and B. C. Shi, Phys. Rev. E **83**, 036707 (2011).
[28] Q. Lou, Z. L. Guo, and B. C. Shi, Europhys. Lett. **99**, 64005 (2012).
[29] M. E. McCracken and J. Abraham, Phys. Rev. E **71**, 036701 (2005).
[30] H. W. Zheng, C. Shu, and Y. T. Chew, Phys. Rev. E **72**, 056705 (2005).
[31] H. W. Zheng, C. Shu, and Y. T. Chew, J. Comput. Phys. **218**, 353 (2006).
[32] A. Fakhari and M. H. Rahimian, Phys. Rev. E **81**, 036707 (2010).
[33] J. J. Huang, C. Shu, and Y. T. Chew, Int. J. Numer. Methods Fluids **60**, 203 (2009).
[34] Y. Q. Zu and S. He, Phys. Rev. E **87**, 043301 (2013).
[35] V. M. Kendon, M. E. Cates, I. Pagonabarraga, J.-C. Desplat, and P. Bladon, J. Fluid Mech. **440**, 147 (2001).
[36] V. E. Badalassi, H. D. Ceniceros, and S. Banerjee, J. Comput. Phys. **190**, 371 (2003).
[37] H. Ding, P. D. M. Spelt, and C. Shu, J. Comput. Phys. **226**, 2078 (2007).
[38] Q. Li, K. H. Luo, Y. J. Gao, and Y. L. He, Phys. Rev. E **85**, 026704 (2012).
[39] B. C. Shi and Z. L. Guo, Phys. Rev. E **79**, 016701 (2009).
[40] Z. H. Chai and T. S. Zhao, Phys. Rev. E **87**, 063309 (2013).

[41] P. Lallemand and L. S. Luo, Phys. Rev. E **61**, 6546 (2000).
[42] B. Chopard, J. L. Falcone, and J. Latt, Eur. Phys. J. Spec. Top. **171**, 245 (2009).
[43] Z. H. Chai and T. S. Zhao, Phys. Rev. E **86**, 016705 (2012).
[44] S. T. Zalesak, J. Comput. Phys. **31**, 335 (1979).
[45] J. B. Bell, P. Colella, and H. M. Glaz, J. Comput. Phys. **85**, 257 (1989).
[46] W. J. Rider and D. B. Kothe, J. Comput. Phys. **141**, 112 (1998).
[47] M. Rudman, Int. J. Numer. Methods Fluids **24**, 671 (1997).
[48] Z. Yu and L. S. Fan, Phys. Rev. E **82**, 046708 (2010).
[49] L. Rayleigh, Proc. London Math. Soc. **14**, 170 (1883); G. I. Taylor, Proc. R. Soc. London **201**, 192 (1950).
[50] B. A. Remington, R. P. Drake, and D. D. Ryutov, Rev. Mod. Phys. **78**, 755 (2006).
[51] J. D. Lindl *et al.*, Phys. Plasmas **11**, 339 (2004).
[52] J. T. Waddell, C. E. Niederhaus, and J. W. Jacobs, Phys. Fluids **13**, 1263 (2001).
[53] S. Chandrasekhar, *Hydrodynamic and Hydromagnetic Stability* (Oxford University Press, Oxford, 1961).
[54] R. Menikoff, R. C. Mjolsness, D. H. Sharp, and C. Zemach, Phys. Fluids **20**, 2000 (1977).
[55] V. N. Goncharov, Phys. Rev. Lett. **88**, 134502 (2002).
[56] R. Banerjee, L. Mandal, S. Roy, M. Khan, and M. R. Guptae, Phys. Plasmas **18**, 022109 (2011).
[57] G. Tryggvason, J. Comput. Phys. **75**, 253 (1988).
[58] X. He, R. Zhang, S. Chen, and G. D. Doolen, Phys. Fluids **11**, 1143 (1999).
[59] J. L. Guermond and L. Quartapelle, J. Comput. Phys. **165**, 167 (2000).
[60] A. Celani, A. Mazzino, P. Muratore-Ginanneschi, and L. Vozella, J. Fluid Mech. **622**, 115 (2009).
[61] M. S. Shadloo, A. Zainali, and M. Yildiz, Comput. Mech. **51**, 699 (2013).
[62] T. Wei and D. Livescu, Phys. Rev. E **86**, 046405 (2012).
[63] R. S. Scorer, J. Fluid Mech. **2**, 583 (1957).
[64] J. Glimm, X. L. Li, and An-Der Lin, Acta Math. Appl. Sin. **18**, 1 (2002).
[65] P. Ramaprabhu, G. Dimonte, Y. N. Young, A. C. Calder, and B. Fryxell, Phys. Rev. E **74**, 066308 (2006).